SIAM J. SCI. COMPUT.
Vol. 40, No. 1, pp. B110–B137

DECOUPLED, LINEAR, AND ENERGY STABLE FINITE ELEMENT METHOD FOR THE CAHN–HILLIARD–NAVIER–STOKES–DARCY PHASE FIELD MODEL*

YALI GAO†, XIAOMING HE‡, LIQUAN MEI†, AND XIAOFENG YANG§

Abstract. In this paper, we consider the numerical approximation for a phase field model of the coupled two-phase free flow and two-phase porous media flow. This model consists of Cahn–Hilliard–Navier–Stokes equations in the free flow region and Cahn–Hilliard–Darcy equations in the porous media region that are coupled by seven interface conditions. The coupled system is decoupled based on the interface conditions and the solution values on the interface from the previous time step. A fully discretized scheme with finite elements for the spatial discretization is developed to solve the decoupled system. In order to deal with the difficulties arising from the interface conditions, the decoupled scheme needs to be constructed appropriately for the interface terms, and a modified discrete energy is introduced with an interface component. Furthermore, the scheme is linearized and energy stable. Hence, at each time step one need only solve a linear elliptic system for each of the two decoupled equations. Stability of the model and the proposed method is rigorously proved. Numerical experiments are presented to illustrate the features of the proposed numerical method and verify the theoretical conclusions.

Key words. Cahn–Hilliard–Navier–Stokes–Darcy, diffuse interface, finite element method, energy stability

AMS subject classifications. 65M60, 65M12, 65M15, 35M10, 35Q35, 76D07, 76S05

DOI. 10.1137/16M1100885

1. Introduction.

The Stokes–Darcy (or Navier–Stokes–Darcy) problem is a coupled problem of free incompressible fluid flow together with the flow through a porous media region. This type of coupled flow is often involved in many applications, such as groundwater systems [18, 29, 57, 65], industrial filtrations [35, 54], petroleum extraction [2, 3, 19, 58], biochemical transport [27], etc. The model couples the Stokes (or Navier–Stokes) equation and Darcy's law through some interface conditions, enabling a better description of the physics of these applications compared with the Darcy's law by itself. Therefore, many numerical methods have been developed for solving the Stokes–Darcy model, such as iterative domain decomposition methods [7, 13, 14, 21, 30, 31, 32, 55, 94], noniterative domain decomposition methods [15, 38, 46], Lagrange multiplier methods [4, 42, 43, 66], discontinuous Galerkin methods [44, 61, 68, 83], multigrid methods [10, 11, 76], partitioned time stepping methods [77, 84], coupled finite element methods [12, 16, 62, 74], mortar finite element methods [36, 40, 45], boundary integral methods [6, 93], least square methods [34, 78], finite volume methods [67, 95], and so on.

*Submitted to the journal's Computational Methods in Science and Engineering section October 27, 2016; accepted for publication (in revised form) October 26, 2017; published electronically January 24, 2018.

http://www.siam.org/journals/sisc/40-1/M110088.html

Funding: This work was partially supported by NSF grants DMS-1418624, DMS-1418898, and DMS-1720212, the National Science Foundation of China (11371289), and the China Scholarship Council (201506280175).

†School of Mathematics and Statistics, Xi'an Jiaotong University, Xi'an, 710049, China (gaoyli2008@163.com, lqmei@mail.xjtu.edu.cn).

‡Corresponding author. Department of Mathematics and Statistics, Missouri University of Science and Technology, Rolla, MO 65409 (hex@mst.edu).

§Department of Mathematics, University of South Carolina, Columbia, SC 29208 (xfyang@math.sc.edu), and School of Mathematical Sciences, University of Electronic Science and Technology of China, Chengdu 610054, China.

However, most of the existing works on the Stokes–Darcy model are devoted to single-phase flows, and hence they cannot be used for the applications of multiphase flow. Recently, researchers [19, 28, 48, 51, 53] started to develop the models to couple the porous media flow with the two-phase free flow, for which the phase field method is adopted. In [19], Chen, Sun, and Wang utilized the Cahn–Hilliard–Navier–Stokes (CHNS) equation to govern the two-phase fluid system, and the two-phase Darcy's law for the two-phase porous medium flow. The coupling between these two equations is through the interface conditions including the generalized Navier boundary condition [80, 81, 82]. In [28], a modified Cahn–Hilliard equation is coupled with an unsteady Darcy-Stokes model, which uses the same equation with different coefficients for both Darcy and Stokes flows without interface transmission conditions. In [48, 51, 53], a Cahn–Hilliard–Stokes–Darcy (CHSD) system and a Cahn–Hilliard–Navier–Stokes–Darcy (CHNSD) system are developed for two-phase incompressible flows in the karstic geometry. It is remarkable that the CHNS equation is utilized to govern the two-phase free fluid, which is similar to [19]. However, in the porous media region, the Cahn–Hilliard–Darcy (CHD) equation is used instead of the two-phase Darcy's law. Therefore, the interface conditions in [48, 51, 53] couple these two equations together that are different from those of [19]. Furthermore, two coupled, unconditionally stable numerical algorithms, which combine two Cahn–Hilliard equations in the Stokes and Darcy domains into one Cahn–Hilliard equation on the whole domain, are proposed and analyzed for the CHSD system in [48]. A "partially" decoupled and nonlinear scheme, which still directly solves one Cahn–Hilliard equation on the whole domain but decouples the Stokes and Darcy equations, was also proposed for the CHSD system in [48]. In this paper, we propose a decoupled, linear and unconditionally stable finite element method to solve a CHNSD model which is based on the model proposed in [51]. To the best of our knowledge, this is the first numerical method proposed for the CHNSD model and the basic ideas of this method have significant differences from those of the existing numerical methods for the CHSD model (see Remark 3.5).

It is remarkable that, in all existing literature for the system that couples the two-phase free fluid flow with two-phase porous media flow [19, 28, 48, 51, 53], the phase field method is adopted to simulate the free interface motions between two immiscible fluids. This is because of its exceptional versatility in modeling and numerical simulations. In this approach, the interface is represented by a thin but smooth transition layer that removes the singularities at the interface. Such a model permits us to solve the problem by integrating a set of PDEs for the whole system, thus avoiding the explicit treatment of the boundary conditions at the interface. Nowadays, the phase field method has been used successfully in many fields of science and engineering to describe multiphasic materials and emerged as one of the most effective modeling and computational tools to study interfacial phenomena; see [1, 24, 39, 47, 56, 59, 60, 63, 64, 70, 72, 103] and the references therein.

To construct the numerical schemes for the typical Cahn–Hilliard phase field models coupled with the hydrodynamics, one of the most challenging issue is how to develop proper temporal discretization for the nonlinear terms in order to preserve energy stability at the time-discrete level, where the main difficulties include (i) the coupling between the velocity and phase function through the convection term in the phase equation and nonlinear stress in the momentum equation; (ii) the coupling of the velocity and pressure through the incompressibility constraint; and (iii) the stiffness of the phase equation associated with the interfacial width. For the CHNSD model, the difficulties are further increased to a large extent due to the various interface

conditions between the two-phase free flow and the two-phase porous media flow.

Therefore, the main purpose of this paper is to construct a fully discretized scheme for solving the CHNSD model which (a) is unconditionally stable, (b) has a discrete energy stability, and (c) leads to decoupled linear equations to solve at each time step. This is by no means an easy task due to highly nonlinear couplings between velocity, pressure, phase function, and various interface conditions. The mathematical analysis for the model and the proposed numerical method does not hold if one simply combines available approaches for the CHNS and CHD models. In order to deal with the difficulties arising from the interface conditions for the energy stability, the decoupled scheme needs to be constructed appropriately for the interface terms and a modified discrete energy is introduced with an interface component. Since our scheme decouples the CHNS equation and CHD equation from the originally coupled model, it does not follow the idea of the schemes in [48] which directly solve one Cahn–Hilliard equation on the whole domain, and hence it needs different treatment for the interface conditions.

The outline of this paper is as follows. In the next section, a time-dependent CHNSD model is provided with its weak formulation and energy law. Section 3 is devoted to the decoupled, linearized, and energy stable finite element method and its energy stability. In section 4, four numerical experiments are presented to illustrate the features of the model and the numerical method. Finally, a brief conclusion is given in the last section.

2. Cahn–Hilliard–Navier–Stokes–Darcy model. In this section, we give a brief introduction to the CHNSD model, present the weak formulation, and show the dissipative energy law in the PDE level.

2.1. Model system. We consider a bounded domain $\Omega = \Omega_c \bigcup \Omega_m \subset \mathbb{R}^d$, $(d = 2, 3)$ where Ω_c is the free flow region and Ω_m is the porous media region. Let $\partial\Omega_c$ and $\partial\Omega_m$, which are assumed to be Lipschitz continuous, denote the boundaries of Ω_c and Ω_m, respectively. Let $\Gamma = \partial\Omega_m \cap \partial\Omega_c$, $\Gamma_m = \partial\Omega_m \backslash \Gamma$, and $\Gamma_c = \partial\Omega_c \backslash \Gamma$. A two-dimensional geometry is illustrated in Figure 1.

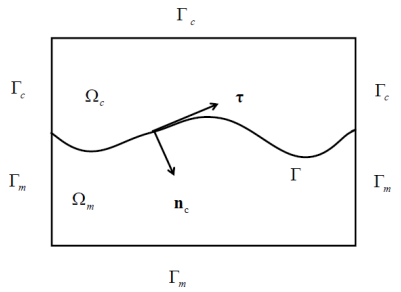

FIG. 1. *A sketch of the porous median domain Ω_m, fluid domain Ω_c, and the interface Γ.*

Let w_j $(j = c, m)$ denote the chemical potential of the binary mixture associated to phase function ϕ which is given by the variational derivative of the free energy functional and allows for the description of the interface between the two materials by a continuously varying concentration profile [23]. The parameter M_j $(j = c, m)$ is a diffusion coefficient which is called mobility and may depend on phase function ϕ, but is here taken constant for simplicity. Define $f(\phi) = F'(\phi)$ where $F(\phi)$ represents the Helmholtz free energy and is usually taken to be a nonconvex function of ϕ for immiscible two-phase flows. In this article, we consider a double-well polynomial of

Ginzburg–Landau type: $F(\phi) = \frac{1}{4\epsilon}(\phi^2 - 1)^2$ implies the hydro-phobic type (tendency of separation) of interactions [50, 90, 98, 106]. Furthermore, γ and ϵ denote the elastic relaxation time and the capillary width of the thin interfacial region. The interfacial region between the phases has a thickness of order $O(\epsilon)$. ϕ_j $(j = c, m)$ represents the phase function in Ω_j $(j = c, m)$, which assumes distinct values in the bulk phases away from a thin interfacial region and varies smoothly over this interfacial region for indicating the fluid phases.

In the porous media region Ω_m, let $\boldsymbol{u}_m$ denote the fluid discharge rate in the porous media, $\mathbb{K}$ denote the hydraulic conductivity tensor that describes the ease in which the fluid can move through the pore space, and p_m denote the hydraulic head. Then the porous media flow is assumed to satisfy the following CHD equations,

$$\mathbb{K}^{-1}\boldsymbol{u}_m = -\nabla p_m + w_m \nabla \phi_m, \tag{1}$$

$$\nabla \cdot \boldsymbol{u}_m = 0, \tag{2}$$

$$\frac{\partial \phi_m}{\partial t} + \boldsymbol{u}_m \cdot \nabla \phi_m - \nabla \cdot (M_m \nabla w_m) = 0, \tag{3}$$

$$w_m + \gamma\epsilon\triangle\phi_m - \gamma f(\phi_m) = 0, \tag{4}$$

where the $w_m \nabla \phi_m$ is the induced extra stress from the free energy. We will consider the following second order formulation via inserting Darcy's law (1) into the mass conservation equation (2),

$$-\nabla \cdot (\mathbb{K}\nabla p_m - \mathbb{K} w_m \nabla \phi_m) = 0. \tag{5}$$

The advantage of the form (5) with respect to (1) and (2) is the elimination of the velocity as an unknown field which is not required in practice. This primal formulation can be employed within the porous media without losing any information. The Darcy velocity can be recovered via (1). We note that velocities $\boldsymbol{u}_m$ computed through (5) and (1) in general do not guarantee mass conservation [75].

In the fluid region Ω_c, let $\boldsymbol{u}_c$ denote the fluid velocity, p_c denote the kinematic pressure, and ν denote the kinematic viscosity of the fluid. Then the fluid flow is assumed to satisfy the Cahn–Hilliard–Navier–Stokes (CHNS) equations

$$\frac{\partial \boldsymbol{u}_c}{\partial t} + (\boldsymbol{u}_c \cdot \nabla)\boldsymbol{u}_c - \nu\triangle\boldsymbol{u}_c + \nabla p_c - w_c \nabla \phi_c = 0, \tag{6}$$

$$\nabla \cdot \boldsymbol{u}_c = 0, \tag{7}$$

$$\frac{\partial \phi_c}{\partial t} + \boldsymbol{u}_c \cdot \nabla \phi_c - \nabla \cdot (M_c \nabla w_c) = 0, \tag{8}$$

$$w_c + \gamma\epsilon\triangle\phi_c - \gamma f(\phi_c) = 0. \tag{9}$$

The Cahn–Hilliard equation (8)–(9) is derived from the energetic point of view by assuming the following phenomenological total free energy $\gamma \int_{\Omega_c} \frac{\epsilon}{2}|\nabla\phi_c|^2 + F(\phi_c))d\boldsymbol{x}$. If one assumes a generalized Ficks law [9] that the mass flux be proportional to the gradient of the chemical potential, then the Cahn–Hilliard equations and Navier–Stokes equations are coupled together via an extra phase induced stress term in the Navier–Stokes equations and a fluid induced transport term in the Cahn–Hilliard equation. The coupled term $w_c \nabla \phi_c$ in the convective Cahn–Hilliard equation (6) can be interpreted as the "elastic" force exerted by the diffusive interface of the two-phase flow, and that also converges to the surface tension at sharp interface limit $\epsilon \to 0$ at least heuristically [53]. The convection term $\boldsymbol{u}_c \cdot \nabla \phi_c$ represents the transport property of the phase function [70].

The CHD system (1)–(4) and CHNS system (6)–(9) are coupled through the following interface conditions. First, the continuity of normal velocity and the balance of force normal to the interface lead to

$$\boldsymbol{u}_c \cdot \mathbf{n}_c = -\boldsymbol{u}_m \cdot \mathbf{n}_m, \tag{10}$$

$$p_c - \nu \mathbf{n}_c \cdot (\nabla \boldsymbol{u}_c \cdot \mathbf{n}_c) = p_m \tag{11}$$

on the interface Γ where $\mathbf{n}_c$ and $\mathbf{n}_m$ denote the unit outer normal to the fluid and the porous media regions at the interface Γ, respectively. Since both of them are in normal directions, the following Beavers–Joseph–Saffman–Jones (BJS) interface condition [5] is imposed in the tangential direction on the interface

$$-\nu \boldsymbol{\tau}_j \cdot (\nabla \boldsymbol{u}_c \cdot \mathbf{n}_c) = \frac{\alpha \nu \sqrt{\mathrm{d}}}{\sqrt{\mathrm{tr}(\chi)}} \boldsymbol{\tau}_j \cdot \boldsymbol{u}_c, \tag{12}$$

where $\boldsymbol{\tau}_j$ $(j = 1, \ldots, d-1)$ denote mutually orthogonal unit tangential vectors to the interface Γ, χ is the permeability matrix of the porous media, $\mathrm{tr}(\chi)$ is its trace.

In addition, the continuity conditions for the phase field function, the chemical potential, and their normal derivatives are imposed on the interface [48, 51, 53],

$$\phi_m = \phi_c, \tag{13}$$

$$w_c = w_m, \tag{14}$$

$$\nabla \phi_c \cdot \mathbf{n}_c = -\nabla \phi_m \cdot \mathbf{n}_m, \tag{15}$$

$$M_c \nabla w_c \cdot \mathbf{n}_c = -M_m \nabla w_m \cdot \mathbf{n}_m. \tag{16}$$

The above system should be supplemented with a set of suitable boundary conditions and initial conditions. For simplicity, we consider

$$p_m|_{\Gamma_m} = 0, \quad \nabla \phi_m \cdot \mathbf{n}_m|_{\Gamma_m} = 0, \quad M_m \nabla w_m \cdot \mathbf{n}_m|_{\Gamma_m} = 0 \tag{17}$$

on Γ_m, and

$$\boldsymbol{u}_c|_{\Gamma_c} = 0, \quad \nabla \phi_c \cdot \mathbf{n}_c|_{\Gamma_c} = 0, \quad M_c \nabla w_c \cdot \mathbf{n}_c|_{\Gamma_c} = 0 \tag{18}$$

on Γ_c. The initial conditions can be simply given as

$$\phi_j(0, \boldsymbol{x}) = \phi_j^0(\boldsymbol{x}), \ j = c, m, \quad \boldsymbol{u}_c(0, \boldsymbol{x}) = \boldsymbol{u}_c^0(\boldsymbol{x}). \tag{19}$$

Without loss of generality, we also assume that the medium Ω_m is isotropic so that $\mathbb{K}$ is a symmetric and positive definite matrix $\mathbb{K} = k\,\mathbb{I}$ where k is a scalar function depending on position $\boldsymbol{x} \in \mathbb{R}^d$, and $\mathbb{I}$ is the identity matrix.

Remark 2.1. In order to derive the corresponding nondimensional model, we first define

$$t_0 = \sqrt{\frac{L_0}{g}}, \quad u_0 = \frac{L_0}{t_0}, \quad p_0 = \rho_0 u_0^2,$$

where L_0 and ρ_0 are the characteristic length of the problem domain and density of the fluid. Table 1 shows the nondimensionalization we obtain with these scalings based on [52, 79].

Substituting these dimensionless variables into the above model, one can derive a nondimensional model. Since the nondimensional model has the same format as the above one except for the "hat" which represents the dimensionless parameters, we can consider the above model as the nondimensional model with the "hat" omitted everywhere.

TABLE 1
The nondimensional parameters for CHNSD system.

Variable	Units	Nondimensionalization
t	s	$\hat{t} = \frac{t}{t_0}$
$\boldsymbol{x}$	m	$\hat{\boldsymbol{x}} = \frac{\boldsymbol{x}}{L_0}$
ν	$Pa \cdot s$ or $kg/(m \cdot s)$	$\hat{\nu} = \frac{\nu t_0}{\rho_0 L_0^2}$
γ	J/m^2 or kg/s^2	$\hat{\gamma} = \frac{\gamma}{\rho_0 L_0 u_0^2}$
ϵ	m	$\hat{\epsilon} = \frac{\epsilon}{L_0}$
$\mathbb{K}$	$m^3 \cdot s/kg$	$\hat{\mathbb{K}} = \frac{\rho_0}{t_0}\mathbb{K}$
$\boldsymbol{u}_m$, $\boldsymbol{u}_c$	m/s	$\hat{\boldsymbol{u}}_m = \frac{\boldsymbol{u}_m}{u_0}$, $\hat{\boldsymbol{u}}_c = \frac{\boldsymbol{u}_c}{u_0}$
p_m, p_c	Pa	$\hat{p}_m = \frac{p_m}{p_0}$, $\hat{p}_c = \frac{p_c}{p_0}$
ω_m, ω_c	J/m^3 or $kg/(m \cdot s^2)$	$\hat{w}_m = \frac{\omega_m}{\rho_0 u_0^2}$, $\hat{w}_c = \frac{\omega_c}{\rho_0 u_0^2}$
M_m, M_c	$m^5/(J \cdot s)$ or $m^3 \cdot s/kg$	$\hat{M}_m = \frac{\rho_0 M_m}{t_0}$, $\hat{M}_c = \frac{\rho_0 M_c}{t_0}$

2.2. The weak formulation. We now provide the weak formulation of the CHNSD model system (1)–(16). We use the standard notation for the Sobolev space $W^{m,k}(\Omega)$, where m is a nonnegative integer and $1 \le k \le \infty$. Let $H^m(\Omega) = W^{m,2}(\Omega)$ with the norm $\|\cdot\|_m$ and seminorm $|\cdot|$. The norm $\|\cdot\|_\infty$ denotes the essential supremum. For simplification, we denote L^2 norm $\|\cdot\|_0$ by $\|\cdot\|$. Set $\boldsymbol{V} = [H_0^1(\Omega)]^d = \{\boldsymbol{v} \in [H^1(\Omega)]^d : \boldsymbol{v}|_{\partial\Omega} = 0\}$. Define the space

$$\dot{L}^2(\Omega_j) := \left\{ v \in L^2(\Omega_j) : \int_{\Omega_j} v d\boldsymbol{x} = 0 \right\}.$$

Furthermore, we denote $\dot{H}^1(\Omega_j) = H^1(\Omega_j) \cap \dot{L}^2(\Omega_j)$, which is a Hilbert space with inner product $(u, v)_{H^1} = \int_{\Omega_j} \nabla u \cdot \nabla v \, d\boldsymbol{x}$ due to the classical Poincaré inequality for functions with zero mean. Its dual space is simply denoted by $(\dot{H}^1(\Omega_j))'$. For our coupled system, the spaces that we utilize are

$$\begin{aligned}
\boldsymbol{X}_m &= \{\boldsymbol{v} \in [H^1(\Omega_m)]^d, \boldsymbol{v} = 0 \text{ on } \Gamma_m\},\\
\boldsymbol{X}_c &= \{\boldsymbol{v} \in [H^1(\Omega_c)]^d, \boldsymbol{v} = 0 \text{ on } \Gamma_c\},\\
\boldsymbol{Y}_c &= \{\boldsymbol{v} \in [H^1(\Omega_c)]^d\},\\
\boldsymbol{X}_{c,div} &= \{\boldsymbol{v} \in \boldsymbol{X}_c, \nabla \cdot \boldsymbol{v} = 0\},\\
Q_j = \dot{H}^1(\Omega_j), &\quad Y_j = H^1(\Omega_j), \quad j = c, m.
\end{aligned}$$

P_τ denotes the projection onto the tangent space on Γ, i.e.,

$$P_\tau \boldsymbol{u} = \sum_{j=1}^{d-1} (\boldsymbol{u} \cdot \boldsymbol{\tau}_j)\boldsymbol{\tau}_j.$$

For the domain Ω_j $(j = c, m)$, $(\cdot, \cdot)$ denotes the L^2 inner product on the domain Ω_j determined by the subscript of integrated functions, and $\langle \cdot, \cdot \rangle$ denotes the L^2 inner product on the interface Γ.

By plugging (1) into (2) and (3) and applying the seven interface conditions (10)–(16), the weak formulation of the proposed CHNSD is given as follows: find

$$(p_m, \phi_m, w_m, \boldsymbol{u}_c, p_c, \phi_c, w_c) \in (Q_m, Y_m, Y_m, \boldsymbol{X}_c, Q_c, Y_c, Y_c)$$

such that

$$(\mathbb{K}\nabla p_m, \nabla q) - (\mathbb{K} w_m \nabla \phi_m, \nabla q) - \langle \boldsymbol{u}_c \cdot \mathbf{n}_c, q\rangle = 0 \ \forall\ q \in Q_m, \tag{20}$$

$$\begin{aligned}&\left(\frac{\partial \phi_m}{\partial t}, \psi\right) - (\mathbb{K}\nabla p_m \cdot \nabla \phi_m, \psi) + (\mathbb{K} w_m \nabla \phi_m \cdot \nabla \phi_m, \psi)\\ &+(M_m \nabla w_m, \nabla \psi) + \langle M_c \nabla w_c \cdot \mathbf{n}_c, \psi\rangle + \langle \phi_m - \phi_c, \psi\rangle = 0 \ \forall\ \psi \in Y_m,\end{aligned} \tag{21}$$

$$\begin{aligned}&(w_m, \omega) - \gamma\epsilon(\nabla \phi_m, \nabla \omega) - \gamma(f(\phi_m), \omega) - \gamma\epsilon\langle \nabla \phi_c \cdot \mathbf{n}_c, \omega\rangle\\ &+\langle w_m - w_c, \omega\rangle = 0 \ \forall\ \omega \in Y_m,\end{aligned} \tag{22}$$

$$\begin{aligned}&\left(\frac{\partial \boldsymbol{u}_c}{\partial t}, \boldsymbol{v}\right) + ((\boldsymbol{u}_c \cdot \nabla)\, \boldsymbol{u}_c, \boldsymbol{v}) + \nu(\nabla \boldsymbol{u}_c, \nabla \boldsymbol{v}) - (p_c, \nabla \cdot \boldsymbol{v}) - (w_c \nabla \phi_c, \boldsymbol{v})\\ &+\langle p_m, \boldsymbol{v} \cdot \mathbf{n}_c\rangle + \frac{\alpha\nu\sqrt{\mathrm{d}}}{\sqrt{\mathrm{tr}(\chi)}}\langle P_\tau \boldsymbol{u}_c, P_\tau \boldsymbol{v}\rangle = 0 \ \forall\ \boldsymbol{v} \in \boldsymbol{X}_c,\end{aligned} \tag{23}$$

$$(\nabla \cdot \boldsymbol{u}_c, q) = 0 \ \forall\ q \in Q_c, \tag{24}$$

$$\begin{aligned}&\left(\frac{\partial \phi_c}{\partial t}, \psi\right) + (\boldsymbol{u}_c \cdot \nabla \phi_c, \psi) + (M_c \nabla w_c, \nabla \psi) + \langle M_m \nabla w_m \cdot \mathbf{n}_m, \psi\rangle\\ &+\langle \phi_c - \phi_m, \psi\rangle = 0 \ \forall\ \psi \in Y_c,\end{aligned} \tag{25}$$

$$\begin{aligned}&(w_c, \omega) - \gamma\epsilon(\nabla \phi_c, \nabla \omega) - \gamma(f(\phi_c), \omega)\\ &- \gamma\epsilon\langle \nabla \phi_m \cdot \mathbf{n}_m, \omega\rangle + \langle w_c - w_m, \omega\rangle = 0 \ \forall\ \omega \in Y_c,\end{aligned} \tag{26}$$

where $t \in [0, T]$, $\boldsymbol{u}_c \in L^\infty(0, T; [L^2(\Omega_c)]^d) \cap L^2(0, T; \boldsymbol{X}_{c,div})$, $\frac{\partial \boldsymbol{u}_c}{\partial t} \in L^2(0, T; \boldsymbol{X}'_{c,div})$, $p_j \in L^2(0, T; Q_j)$, $\phi_j \in L^\infty(0, T; Y_j) \cap L^2(0, T; H^3(\Omega_j))$, $\frac{\partial \phi_j}{\partial t} \in L^2(0, T; Y'_j)$, $w_j \in L^2(0, T; Y_j)$, and $j = \{c, m\}$. Unlike the idea in [48] which directly solve one Cahn–Hilliard equation on the whole domain, we consider the two Cahn–Hilliard equations on Ω_m and Ω_c separately with appropriate treatment for the interface conditions (13)–(16). The other three interface conditions (10)–(12) are utilized in the traditional way for the single-phase Naiver–Stokes–Darcy model in the literature.

After the above system is solved, $\boldsymbol{u}_m$ can be defined by

$$(\boldsymbol{u}_m, \boldsymbol{v}) = (\mathbb{K}(-\nabla p_m + w_m \nabla \phi_m), \boldsymbol{v}) \ \forall\ \boldsymbol{v} \in \boldsymbol{X}_m, \tag{27}$$

based on (1).

2.3. A dissipative energy law. An important feature of the above weak formulation is that it obeys a dissipative energy law. To this end, we denote the total energy of the coupled system as

$$\begin{aligned}E(\boldsymbol{u}_c, \phi_c, \phi_m) = &\int_{\Omega_c} \frac{1}{2}|\boldsymbol{u}_c|^2 d\boldsymbol{x} + \gamma \int_{\Omega_c} \left(\frac{\epsilon}{2}|\nabla \phi_c|^2 + F(\phi_c)\right) d\boldsymbol{x}\\ &+ \gamma \int_{\Omega_m} \left(\frac{\epsilon}{2}|\nabla \phi_m|^2 + F(\phi_m)\right) d\boldsymbol{x}.\end{aligned} \tag{28}$$

In order to deal with the nonlinear term $(\boldsymbol{u}_c \cdot \nabla)\boldsymbol{u}_c$, we recall the following inequalities [17, 44]: there exist constants C_1 and $\tilde{C}_4$ depending only on Ω_c, such that

for $\boldsymbol{v} \in \boldsymbol{V}$,

$$|\boldsymbol{v}| \le C_1 \|\nabla \boldsymbol{v}\|, \quad \|\boldsymbol{v}\|_{L^4} \le \tilde{C}_4 |\boldsymbol{v}|. \tag{29}$$

Owing to the works in [17, 44], we have the following lemma.

LEMMA 2.2. *Assume that $\boldsymbol{u}_c$ satisfies the following smallness condition:*

$$\|\nabla \boldsymbol{u}_c\| \le \frac{\nu}{2C_1^3 \tilde{C}_4^2} \quad \forall t \in [0, T]. \tag{30}$$

Then, we have the estimate

$$|((\boldsymbol{u}_c \cdot \nabla)\boldsymbol{v}, \boldsymbol{v})| \le \frac{\nu}{2} \|\nabla \boldsymbol{v}\|^2 \ \forall \ \boldsymbol{v} \in \boldsymbol{V}. \tag{31}$$

Proof. Using Hölder's inequality and (29), we obtain

$$|((\boldsymbol{u}_c \cdot \nabla)\boldsymbol{v}, \boldsymbol{v})| \le \|\boldsymbol{u}_c\|_{L^4} \|\boldsymbol{v}\|_{L^4} |\boldsymbol{v}| \le \tilde{C}_4^2 |\boldsymbol{u}_c| |\boldsymbol{v}|^2 \le C_1^3 \tilde{C}_4^2 \|\nabla \boldsymbol{u}_c\| \|\nabla \boldsymbol{v}\|^2. \tag{32}$$

Combing (30) and (32), we derive (31). ∎

LEMMA 2.3. *Let $(\boldsymbol{u}_m, \boldsymbol{u}_c, \phi_m, \phi_c, w_m, w_c)$ be a smooth solution to the initial boundary value problem (1)–(19). Then $(\boldsymbol{u}_m, \boldsymbol{u}_c, \phi_m, \phi_c, w_m, w_c)$ satisfies the following basic energy law:*

$$\frac{d}{dt} E(\boldsymbol{u}_c, \phi_c, \phi_m) \le -\mathcal{D}(t) \le 0, \tag{33}$$

where the energy dissipation $\mathcal{D}$ is given by

$$\begin{aligned} \mathcal{D}(t) = \frac{\nu}{2} \|\nabla \boldsymbol{u}_c\|^2 + M_c \|\nabla w_c\|^2 + k^{-1} \|\boldsymbol{u}_m\|^2 + M_m \|\nabla w_m\|^2 \\ + \frac{\alpha \nu \sqrt{d}}{\sqrt{tr(\chi)}} \langle P_\tau \boldsymbol{u}_c, P_\tau \boldsymbol{u}_c \rangle. \end{aligned} \tag{34}$$

Proof. For the conduit part, set the test function in (23)–(27) by $\boldsymbol{v} = \boldsymbol{u}_c$, $q = p_c$, $\psi = w_c$, and $\omega = -\frac{\partial \phi_c}{\partial t}$: adding the resultants together, and applying the interface conditions (13) and (14), we get

$$\begin{aligned} &\int_{\Omega_c} \frac{1}{2} \frac{d}{dt} |\boldsymbol{u}_c|^2 d\boldsymbol{x} + \gamma \int_{\Omega_c} \left(\frac{\epsilon}{2} \frac{d}{dt} |\nabla \phi_c|^2 + \frac{d}{dt} F(\phi_c) \right) d\boldsymbol{x} + ((\boldsymbol{u}_c \cdot \nabla)\boldsymbol{u}_c, \boldsymbol{u}_c) \\ &\quad + \nu \|\nabla \boldsymbol{u}_c\|^2 + M_c \|\nabla w_c\|^2 + \frac{\alpha \nu \sqrt{\mathrm{d}}}{\sqrt{\mathrm{tr}(\chi)}} \langle P_\tau \boldsymbol{u}_c, P_\tau \boldsymbol{u}_c \rangle \\ &\quad + \langle M_m \nabla w_m \cdot \mathbf{n}_m, w_c \rangle + \gamma \epsilon \left\langle \nabla \phi_m \cdot \mathbf{n}_m, \frac{d}{dt} \phi_c \right\rangle + \langle \boldsymbol{u}_c \cdot \mathbf{n}_c, p_m \rangle = 0. \end{aligned} \tag{35}$$

Using inequality (31) for the above trilinear term $((\boldsymbol{u}_c \cdot \nabla)\boldsymbol{u}_c, \boldsymbol{u}_c)$, we obtain

$$\begin{aligned} &\frac{d}{dt} \int_{\Omega_c} \frac{1}{2} |\boldsymbol{u}_c|^2 d\boldsymbol{x} + \gamma \frac{d}{dt} \int_{\Omega_c} \left(\frac{\epsilon}{2} |\nabla \phi_c|^2 + F(\phi_c) \right) d\boldsymbol{x} \\ &\quad + \frac{\nu}{2} \|\nabla \boldsymbol{u}_c\|^2 + M_c \|\nabla w_c\|^2 + \frac{\alpha \nu \sqrt{\mathrm{d}}}{\sqrt{\mathrm{tr}(\chi)}} \langle P_\tau \boldsymbol{u}_c, P_\tau \boldsymbol{u}_c \rangle \\ &\quad + \langle M_m \nabla w_m \cdot \mathbf{n}_m, w_c \rangle + \gamma \epsilon \left\langle \nabla \phi_m \cdot \mathbf{n}_m, \frac{d}{dt} \phi_c \right\rangle + \langle \boldsymbol{u}_c \cdot \mathbf{n}_c, p_m \rangle \le 0. \end{aligned} \tag{36}$$

Next, we consider the matrix part. By taking $q = p_m$ and $\psi = w_m$ in (20) and (21), respectively, adding these two equations, and applying (27), we obtain

$$\left(\frac{\partial \phi_m}{\partial t}, w_m\right) + (\boldsymbol{u}_m \cdot \nabla \phi_m, w_m) - (\boldsymbol{u}_m, \nabla p_m) + M_m \|\nabla w_m\|^2 + \langle M_c \nabla w_c \cdot \mathbf{n}_c, w_m \rangle - \langle \boldsymbol{u}_c \cdot \mathbf{n}_c, p_m \rangle = 0. \tag{37}$$

By taking the inner product of (27) with $\boldsymbol{u}_m$, we have

$$k^{-1} \|\boldsymbol{u}_m\|^2 = -(\nabla p_m, \boldsymbol{u}_m) + (w_m \nabla \phi_m, \boldsymbol{u}_m). \tag{38}$$

By combining (37) and (38), we obtain

$$\left(\frac{\partial \phi_m}{\partial t}, w_m\right) + k^{-1} \|\boldsymbol{u}_m\|^2 + M_m \|\nabla w_m\|^2 + \langle M_c \nabla w_c \cdot \mathbf{n}_c, w_m \rangle - \langle \boldsymbol{u}_c \cdot \mathbf{n}_c, p_m \rangle = 0. \tag{39}$$

By taking $\omega = -\frac{\partial \phi_m}{\partial t}$ in (22) and adding (39), we derive

$$\gamma \frac{d}{dt} \int_{\Omega_m} \left(\frac{\epsilon}{2} |\nabla \phi_m|^2 + F(\phi_m) \right) d\boldsymbol{x} + k^{-1} \|\boldsymbol{u}_m\|^2 + M_m \|\nabla w_m\|^2 + \langle M_c \nabla w_c \cdot \mathbf{n}_c, w_m \rangle + \gamma \epsilon \left\langle \nabla \phi_c \cdot \mathbf{n}_c, \frac{d}{dt} \phi_m \right\rangle - \langle \boldsymbol{u}_c \cdot \mathbf{n}_c, p_m \rangle = 0. \tag{40}$$

After combining (36) and (40) and applying the interface conditions (13)–(16), we obtain (33). ∎

3. Fully discretized numerical scheme. In this section, we present the fully discretized scheme for the weak formulation (20)–(27) while finite elements are used for the spatial discretization.

There are two popular approaches to handle the nonconvex double-well potential $F(\phi)$. One is the convex splitting method (cf. [33, 37]). The other one is the stabilization method (cf. [20, 71, 73, 85, 87, 88, 89, 90, 91, 92, 96, 97, 99, 100, 101, 102, 104, 105, 107]). In this article we utilize the second one, which does not require solving a nonlinear equation. The unconditional stability of the stabilization method requires that the second derivative of $F(\phi)$ be bounded. However, this is not satisfied by the Ginzburg–Laudau potential, since we are only interested in $\phi \in [-1, 1]$, and it is proved by [8] that a truncated $F(\phi)$ with quadratic growth at infinity also guarantees the boundless of ϕ in the Cahn–Hilliard equation. So it is a common practice to modify $F(\phi)$ to have a quadratic glowth rate for $|\phi| > 1$ (see, e.g., [26, 88]). Without loss of generality, we introduce the following $\hat{F}(\phi)$ to replace $F(\phi)$:

$$\hat{F}(\phi) = \frac{1}{4\epsilon} \begin{cases} 4(\phi+1)^2 & \text{if } \phi < -1, \\ (\phi^2-1)^2 & \text{if } -1 \le \phi \le 1, \\ 4(\phi-1)^2 & \text{if } \phi > 1. \end{cases} \tag{41}$$

Correspondingly, we define $\hat{f}(\phi) = \hat{F}'(\phi)$ and

$$L := \max_{\phi \in \mathbb{R}} |\hat{f}'(\phi)| = \frac{2}{\epsilon}. \tag{42}$$

For convenience, we replace the functions $\hat{f}$ and $\hat{F}$ by f and F by neglecting the symbol $\hat{}$.

Let $\Im_h$ be a quasi-uniform regular partition of triangular element of domain Ω of mesh size h. Suppose we have finite element spaces $Y_{jh} \subset Y_j$, $\boldsymbol{X}_{ch} \subset \boldsymbol{X}_c$, $\boldsymbol{Y}_{ch} \subset \boldsymbol{Y}_c$, and $Q_{jh} \subset Q_j$ with $j = c, m$. Here we assume $\boldsymbol{X}_{ch} \subset \boldsymbol{X}_c$ and $Q_{ch} \subset Q_c$ satisfy the following inf-sup condition for the divergence operator.

There exists a constant $C > 0$ independent of h such that the following LBB condition holds:

$$\inf_{0\neq q_h} \sup_{0\neq \boldsymbol{v}_h} \frac{(\nabla \cdot \boldsymbol{v}_h, q_h)}{\|\boldsymbol{v}_h\|_1} > C \|q_h\| \ \forall\ q_h \in Q_{ch}, \boldsymbol{v}_h \in \boldsymbol{X}_{ch}.$$

Then the semidescretization formulation of the system (20)–(27) is to find

$$(p_{mh}, \phi_{mh}, w_{mh}, \boldsymbol{u}_{ch}, p_{ch}, \phi_{ch}, w_{ch}) \in (Q_{mh}, Y_{mh}, Y_{mh}, \boldsymbol{X}_{ch}, Q_{ch}, Y_{ch}, Y_{ch})$$

such that

$$\begin{aligned}
&(\mathbb{K}\nabla p_{mh}, \nabla q_h) - (\mathbb{K} w_{mh}\nabla\phi_{mh}, \nabla q_h)\\
&\qquad - \langle \boldsymbol{u}_{ch}\cdot \mathbf{n}_c, q_h\rangle = 0 \ \forall\ q_h \in Q_{mh},\\
&\left(\frac{\partial \phi_{mh}}{\partial t}, \psi_h\right) - (\mathbb{K}\nabla p_{mh}\cdot\nabla\phi_{mh}, \psi_h) + (\mathbb{K} w_{mh}\nabla\phi_{mh}\cdot\nabla\phi_{mh}, \psi_h) \qquad (43)\\
&\qquad + (M_m\nabla w_{mh}, \nabla\psi_h) + \langle M_c\nabla w_{ch}\cdot\mathbf{n}_c, \psi_h\rangle \qquad (44)\\
&\qquad + \langle \phi_{mh} - \phi_{ch}, \psi_h\rangle = 0 \ \forall\ \psi_h \in Y_{mh}, \qquad (45)\\
&(w_{mh}, \omega_h) - \gamma\epsilon(\nabla\phi_{mh}, \nabla\omega_h) - \gamma(f(\phi_{mh}), \omega_h) - \gamma\epsilon\langle\nabla\phi_{ch}\cdot\mathbf{n}_c, \omega_h\rangle\\
&\qquad + \langle w_{mh} - w_{ch}, \omega_h\rangle = 0 \ \forall\ \omega_h \in Y_{mh}, \qquad (46)\\
&\left(\frac{\partial \boldsymbol{u}_{ch}}{\partial t}, \boldsymbol{v}_h\right) + ((\boldsymbol{u}_{ch}\cdot\nabla)\,\boldsymbol{u}_{ch}, \boldsymbol{v}_h) + \nu(\nabla\boldsymbol{u}_{ch}, \nabla\boldsymbol{v}_h) - (p_{ch}, \nabla\cdot\boldsymbol{v}_h)\\
&\qquad - (w_{ch}\nabla\phi_{ch}, \boldsymbol{v}_h)\\
&\qquad + \langle p_{mh}, \boldsymbol{v}_h\cdot\mathbf{n}_c\rangle + \frac{\alpha\nu\sqrt{\mathrm{d}}}{\sqrt{\mathrm{tr}(\chi)}}\langle P_\tau\boldsymbol{u}_{ch}, P_\tau\boldsymbol{v}_h\rangle = 0 \ \forall\ \boldsymbol{v}_h \in \boldsymbol{X}_{ch}, \qquad (47)\\
&(\nabla\cdot\boldsymbol{u}_{ch}, q_h) = 0 \ \forall q_h \in Q_{ch}, \qquad (48)\\
&\left(\frac{\partial \phi_{ch}}{\partial t}, \psi_h\right) + (\boldsymbol{u}_{ch}\cdot\nabla\phi_{ch}, \psi_h) + (M_c\nabla w_{ch}, \nabla\psi_h) + \langle M_m\nabla w_{mh}\cdot\mathbf{n}_m, \psi_h\rangle\\
&\qquad + \langle \phi_{ch} - \phi_{mh}, \psi_h\rangle = 0 \ \forall\ \psi_h \in Y_{ch}, \qquad (49)\\
&(w_{ch}, \omega_h) - \gamma\epsilon(\nabla\phi_{ch}, \nabla\omega_h) - \gamma(f(\phi_{ch}), \omega_h) - \gamma\epsilon\langle\nabla\phi_{mh}\cdot\mathbf{n}_m, \omega_h\rangle\\
&\qquad + \langle w_{ch} - w_{mh}, \omega_h\rangle = 0 \ \forall\ \omega_h \in Y_{ch}. \qquad (50)
\end{aligned}$$

Remark 3.1. The analysis for the energy stability of the semidiscrete scheme is similar to the previous PDE energy law, and thus we omit the details here.

Let $0 = t_0 < t_1 < \cdots < t_M = T$ be a uniform partition of $[0, T]$ into subintervals $J^n = (t_n, t_{n+1})$, $n = 0, 1, \ldots, M-1$, with time step size $\Delta t = t_{n+1} - t_n = \frac{T}{M}$. Then we propose the following decoupled, linearized, and stabilized full discretization.

Step 1. Find $(\phi_{mh}^{n+1}, w_{mh}^{n+1}) \in Y_{mh} \times Y_{mh}$, such that

$$\begin{aligned}
&\left(\frac{\phi_{mh}^{n+1} - \phi_{mh}^{n}}{\Delta t}, \psi_h\right) - (\mathbb{K}\nabla p_{mh}^{n}\cdot\nabla\phi_{mh}^{n}, \psi_h) + (\mathbb{K} w_{mh}^{n+1}\nabla\phi_{mh}^{n}\cdot\nabla\phi_{mh}^{n}, \psi_h)\\
&\qquad + (M_m\nabla w_{mh}^{n+1}, \nabla\psi_h) + \langle M_c\nabla w_{ch}^{n}\cdot\mathbf{n}_c, \psi_h\rangle\\
&\qquad + \langle \phi_{mh}^{n} - \phi_{ch}^{n}, \psi_h\rangle = 0 \ \forall\ \psi_h \in Y_{mh},
\end{aligned} \qquad (51)$$

$$(w_{mh}^{n+1},\omega_h)-\gamma\epsilon(\nabla\phi_{mh}^{n+1},\nabla\omega_h)-\gamma(\phi_{mh}^{n+1}-\phi_{mh}^{n},\omega_h)-\gamma(f(\phi_{mh}^{n}),\omega_h)$$
$$-\gamma\epsilon\langle\nabla\phi_{ch}^{n}\cdot\mathbf{n}_c,\omega_h\rangle+\langle w_{mh}^{n}-w_{ch}^{n},\omega_h\rangle=0\ \forall\ \omega_h\in Y_{mh}. \tag{52}$$

Step 2. Find $p_{mh}^{n+1}\in Q_{mh}$, such that

$$(\mathbb{K}\nabla p_{mh}^{n+1},\nabla q_h)-(\mathbb{K}w_{mh}^{n+1}\nabla\phi_{mh}^{n},\nabla q_h)-\langle\boldsymbol{u}_{ch}^{n}\cdot\mathbf{n}_c,q_h\rangle=0\ \forall\ q_h\in Q_{mh}. \tag{53}$$

Step 3. Find $(\phi_{ch}^{n+1},w_{ch}^{n+1})\in Y_{ch}\times Y_{ch}$, such that

$$\left(\frac{\phi_{ch}^{n+1}-\phi_{ch}^{n}}{\Delta t},\psi_h\right)+((\boldsymbol{u}_{ch}^{n}+\Delta t w_{ch}^{n+1}\nabla\phi_{ch}^{n})\cdot\nabla\phi_{ch}^{n},\psi_h)+(M_c\nabla w_{ch}^{n+1},\nabla\psi_h)$$
$$+\langle M_m\nabla w_{mh}^{n}\cdot\mathbf{n}_m,\psi_h\rangle+\langle\phi_{ch}^{n+1}-\phi_{mh}^{n+1},\psi_h\rangle=0\ \forall\ \psi_h\in Y_{ch}, \tag{54}$$

$$(w_{ch}^{n+1},\omega_h)-\gamma\epsilon(\nabla\phi_{ch}^{n+1},\nabla\omega_h)-\frac{\gamma}{\epsilon}(\phi_{ch}^{n+1}-\phi_{ch}^{n},\omega_h)-\gamma(f(\phi_{ch}^{n}),\omega_h)$$
$$-\gamma\epsilon\langle\nabla\phi_{mh}^{n}\cdot\mathbf{n}_m,\omega_h\rangle+\langle w_{ch}^{n+1}-w_{mh}^{n+1},\omega_h\rangle=0\ \forall\ \omega_h\in Y_{ch}. \tag{55}$$

Step 4. Find $(\widetilde{\mathbf{u}}_{ch}^{n+1},\boldsymbol{u}_{ch}^{n+1},p_{ch}^{n+1})\in\boldsymbol{X}_{ch}\times\boldsymbol{Y}_{ch}\times Q_{ch}$, such that

$$\left(\frac{\widetilde{\mathbf{u}}_{ch}^{n+1}-\boldsymbol{u}_{ch}^{n}}{\Delta t},\boldsymbol{v}_h\right)+\left((\boldsymbol{u}_{ch}^{n}\cdot\nabla)\,\widetilde{\mathbf{u}}_{ch}^{n+1},\boldsymbol{v}_h\right)+\nu(\nabla\widetilde{\mathbf{u}}_{ch}^{n+1},\nabla\boldsymbol{v}_h)-(w_{ch}^{n+1}\nabla\phi_{ch}^{n},\boldsymbol{v}_h)$$
$$-(p_{ch}^{n},\nabla\cdot\boldsymbol{v}_h)+\langle 2p_{mh}^{n+1}-p_{mh}^{n}-p_{ch}^{n+1}+p_{ch}^{n},\boldsymbol{v}_h\cdot\mathbf{n}_c\rangle$$
$$+\frac{\alpha\nu\sqrt{\mathrm{d}}}{\sqrt{\mathrm{tr}(\chi)}}\langle P_\tau\widetilde{\mathbf{u}}_{ch}^{n+1},P_\tau\boldsymbol{v}_h\rangle$$
$$+\langle(\widetilde{\mathbf{u}}_{ch}^{n+1}-\boldsymbol{u}_{ch}^{n+1})\cdot\mathbf{n}_c,\boldsymbol{v}_h\cdot\mathbf{n}_c\rangle=0\ \forall\ \boldsymbol{v}_h\in\boldsymbol{X}_{ch}, \tag{56}$$

$$\left(\frac{\boldsymbol{u}_{ch}^{n+1}-\widetilde{\mathbf{u}}_{ch}^{n+1}}{\Delta t},\boldsymbol{v}_h\right)+(\nabla(p_{ch}^{n+1}-p_{ch}^{n}),\boldsymbol{v}_h)$$
$$+\langle(\boldsymbol{u}_{ch}^{n+1}-\widetilde{\mathbf{u}}_{ch}^{n+1})\cdot\mathbf{n}_c,\boldsymbol{v}_h\cdot\mathbf{n}_c\rangle=0\ \forall\ \boldsymbol{v}_h\in\boldsymbol{Y}_{ch}, \tag{57}$$

$$(\nabla(p_{ch}^{n+1}-p_{ch}^{n}),\nabla q_h)+\frac{1}{\Delta t}(\nabla\cdot\widetilde{\mathbf{u}}_{ch}^{n+1},q_h)$$
$$+\frac{1}{\Delta t}\langle(\boldsymbol{u}_{ch}^{n+1}-\widetilde{\mathbf{u}}_{ch}^{n+1})\cdot\mathbf{n}_c,q_h\rangle=0\ \forall\ q_h\in Q_{ch}. \tag{58}$$

Remark 3.2. We recall that $f(\phi)=\frac{1}{\epsilon}\phi(\phi^2-1)$, so the explicit treatment of this term usually leads to a severe restriction on the time step Δt when $\epsilon\ll 1$. Thus we introduce in (52) and (55) two *"stabilizing"* terms to improve the stability while preserving the simplicity. It allows us to treat the nonlinear term explicitly without suffering from any time step constraint [86, 87, 88]. Note that this stabilizing term introduces an extra consistent error of order $O(\Delta t)$ in a small region near the interface, but this error is of the same order as the error introduced by treating $f(\phi)$ explicitly, so the overall truncation error is essentially of the same order with or without the stabilizing term. A similar approach is applied in the contact line boundary condition [41, 92]. This stabilization allows us to prove a discrete energy dissipation law together with appropriate treatments of the interface terms which play a key role for interface problems.

Remark 3.3. The time discretization of the Darcy equation can be motivated from the standpoint of operator-splitting (fractional step method) [49] as follows. There are two contributing forces in the Darcy equation: the pressure gradient and capillary force. We recall intermediate velocity

$$\boldsymbol{u}_{mh}^{n+1} = -\mathbb{K}\nabla p_{mh}^{n} + \mathbb{K}w_{mh}^{n+1}\nabla\phi_{mh}^{n}, \tag{59}$$

and the true velocity

$$\widetilde{\mathbf{u}}_{mh}^{n+1} - \boldsymbol{u}_{mh}^{n+1} = -\mathbb{K}(\nabla p_{mh}^{n+1} - \nabla p_{mh}^{n}), \tag{60}$$

$$\nabla\cdot\widetilde{\mathbf{u}}_{mh}^{n+1} = 0, \tag{61}$$

defined in [49]. It is clear that the summation of (59), (60), and (61) will recover (1)–(2). The true velocity $\widetilde{\mathbf{u}}_{mh}^{n+1}$ can be eliminated once one applies the divergence operator to (60),

$$\nabla\cdot\boldsymbol{u}_{mh}^{n+1} = \mathbb{K}\nabla\cdot(\nabla p_{mh}^{n+1} - \nabla p_{mh}^{n}). \tag{62}$$

Taking the inner product of (62) with test function $q_h \in Q_{mh}$, applying the Green's equation, and using (60), we derive

$$\begin{aligned} -(\boldsymbol{u}_{mh}^{n+1}, \nabla q_h) + \langle \boldsymbol{u}_{mh}^{n+1}\cdot\mathbf{n}_m, q_h\rangle &= -\mathbb{K}(\nabla p_{mh}^{n+1} - \nabla p_{mh}^{n}, \nabla q_h) \\ &\quad + \mathbb{K}\langle(\nabla p_{mh}^{n+1} - \nabla p_{mh}^{n})\cdot\mathbf{n}_m, q_h\rangle \\ &= -\mathbb{K}(\nabla p_{mh}^{n+1} - \nabla p_{mh}^{n}, \nabla q_h) \\ &\quad - \langle(\widetilde{\mathbf{u}}_{mh}^{n+1} - \boldsymbol{u}_{mh}^{n+1})\cdot\mathbf{n}_m, q_h\rangle. \end{aligned} \tag{63}$$

In our numerical algorithm, we imposed the interface condition

$$\widetilde{\mathbf{u}}_{mh}^{n+1}\cdot\mathbf{n}_m|_\Gamma = \boldsymbol{u}_{mh}^{n+1}\cdot\mathbf{n}_m|_\Gamma, \tag{64}$$

Thus, applying the interface condition (10) and replacing $\boldsymbol{u}_{ch}^{n+1}$ by $\boldsymbol{u}_{ch}^{n}$ for the decoupling purpose, (64) can be rewritten as

$$-(\boldsymbol{u}_{mh}^{n+1}, \nabla q_h) = -\mathbb{K}(\nabla p_{mh}^{n+1} - \nabla p_{mh}^{n}, \nabla q_h) + \langle \boldsymbol{u}_{ch}^{n}\cdot\mathbf{n}_c, q_h\rangle. \tag{65}$$

Substituting (59) into (65), we derive the finally full discretization (53) of the Darcy equation.

Remark 3.4. For the nonlinear Navier–Stokes equation, we used the pressure-correction idea [87, 90]. We recall

$$\frac{\boldsymbol{u}_{ch}^{n+1} - \widetilde{\mathbf{u}}_{ch}^{n+1}}{\Delta t} + \nabla(p_{ch}^{n+1} - p_{ch}^{n}) = 0, \tag{66}$$

$$\nabla\cdot\boldsymbol{u}_{ch}^{n+1} = 0. \tag{67}$$

First, taking the inner product of (67) with test function $q_h \in Q_{ch}$, using (66), and applying the Green's formulation, we derive

$$\frac{1}{\Delta t}(\nabla\cdot\widetilde{\mathbf{u}}_{ch}^{n+1}, q_h) + (\nabla(p_{ch}^{n+1} - p_{ch}^{n}), \nabla q_h) - \langle\nabla(p_{ch}^{n+1} - p_{ch}^{n})\cdot\mathbf{n}_c, q_h\rangle = 0. \tag{68}$$

Then, using the relation $\nabla(p_{ch}^{n+1} - p_{ch}^{n})\cdot\mathbf{n}_c|_\Gamma = -\frac{1}{\Delta t}(\boldsymbol{u}_{ch}^{n+1} - \widetilde{\mathbf{u}}_{ch}^{n+1})\cdot\mathbf{n}_c|_\Gamma$ due to the fact (66), we derive (58).

In the numerical scheme, we also impose the interface condition

$$\widetilde{\mathbf{u}}_{ch}^{n+1}\cdot\mathbf{n}_c|_\Gamma = \boldsymbol{u}_{ch}^{n+1}\cdot\mathbf{n}_c|_\Gamma \tag{69}$$

in (56) and (57).

Remark 3.5. Comparing the formulations of the above decoupled numerical method with the numerical scheme in [48], the major differences include that (1) our method solves the CHNSD equation while the method in [48] solves the CHSD; (2) our decoupled method solves two Cahn–Hilliard equations in free fluid flow and porous medium regions, respectively, while, in [48], the two Cahn–Hilliard equations are combined into one Cahn–Hilliard equation on the whole domain; (3) our techniques to deal with the stability are different from those in [48], especially for the interface terms and the treatment of the nonconvex double-well potential $F(\phi)$. Therefore, the proposed method requires solving only a linear algebra system at each time step while the method in [48] needs to solve a nonlinear algebra system based on the convex splitting method. Moreover, the method in [48] needs to solve a system for the Cahn–Hilliard equation on the whole problem domain while the proposed method solves two smaller systems for the Cahn–Hilliard equation on the two subdomains separately.

We now prove the energy stability theorem as follows.

THEOREM 3.6. *The approximation* $(\boldsymbol{u}_{mh}^{n+1}, \boldsymbol{u}_{ch}^{n+1}, p_{ch}^{n+1}, \phi_{mh}^{n+1}, \phi_{ch}^{n+1})$ *by the scheme* (51)–(58) *satisfies the following inequality:*

$$
\begin{aligned}
(70)\quad & E^{n+1} - E^n + \frac{1}{2}\Delta t^2[\|\nabla p_{ch}^{n+1}\|^2 - \|\nabla p_{ch}^{n}\|^2] + \frac{1}{2}\Delta t k[\|\nabla p_{mh}^{n+1}\|^2 - \|\nabla p_{mh}^{n}\|^2] \\
& + \Delta t\langle \boldsymbol{u}_{ch}^{n+1}\cdot \mathbf{n}_c, p_{mh}^{n+1}\rangle - \Delta t\langle \boldsymbol{u}_{ch}^{n}\cdot \mathbf{n}_c, p_{mh}^{n}\rangle \le -\mathcal{D}^{n+1},
\end{aligned}
$$

where the E^n *is defined as*

$$
\begin{aligned}
(71)\quad E^n = & \int_{\Omega_c} \frac{1}{2}|\boldsymbol{u}_{ch}^n|^2 d\boldsymbol{x} + \gamma \int_{\Omega_c} \left[\frac{\epsilon}{2}|\nabla \phi_{ch}^n|^2 + F(\phi_{ch}^n)\right] d\boldsymbol{x} \\
& + \gamma \int_{\Omega_m} \left[\frac{\epsilon}{2}|\nabla \phi_{mh}^n|^2 + F(\phi_{mh}^n)\right] d\boldsymbol{x},
\end{aligned}
$$

and the energy dissipation $\mathcal{D}^{n+1}$ *is given by*

$$
\begin{aligned}
(72)\quad \mathcal{D}^{n+1} = & \frac{1}{2}[\|\widetilde{\mathbf{u}}_{ch}^{n+1} - \boldsymbol{u}_\star^n\|^2 + \|\boldsymbol{u}_\star^n - \boldsymbol{u}_{ch}^n\|^2] + \frac{\nu}{2}\Delta t\|\nabla \widetilde{\mathbf{u}}_{ch}^{n+1}\|^2 + \frac{1}{2}\gamma\epsilon\|\nabla \phi_{mh}^{n+1} - \nabla \phi_{mh}^n\|^2 \\
& + \Delta t M_c\|\nabla w_{ch}^{n+1}\|^2 + \Delta t M_m\|\nabla w_{mh}^{n+1}\|^2 + \frac{1}{2}\gamma\epsilon\|\nabla \phi_{ch}^{n+1} - \nabla \phi_{ch}^n\|^2 \\
& + \frac{1}{2}\Delta t k^{-1}[\|\boldsymbol{u}_{mh}^{n+1}\|^2 + \|\widetilde{\mathbf{u}}_{mh}^{n+1}\|^2] + \Delta t\frac{\alpha\nu\sqrt{d}}{\sqrt{tr(\chi)}}\langle P_\tau \widetilde{\mathbf{u}}_{ch}^{n+1}, P_\tau \widetilde{\mathbf{u}}_{ch}^{n+1}\rangle
\end{aligned}
$$

and

$$
(73)\quad \boldsymbol{u}_\star^n = \boldsymbol{u}_{ch}^n + \Delta t w_{ch}^{n+1}\nabla \phi_{ch}^n.
$$

Furthermore, if the following time step constraint is satisfied,

$$
(74)\quad \Delta t \le \frac{k}{2C^2},
$$

where C *is the constant in Lemma* 1 *of* [22]*, the scheme* (51)–(58) *is energy stable.*

Proof. By taking the test function $\boldsymbol{v}_h = \Delta t\widetilde{\mathbf{u}}_{ch}^{n+1}$ in (56), utilizing the trilinear property (31), and combining (73), (69), and the following identity

$$
(75)\quad 2a(a-b) = a^2 - b^2 + (a-b)^2,
$$

we obtain

$$\begin{aligned}\frac{1}{2}(\|\widetilde{\mathbf{u}}_{ch}^{n+1}\|^2-\|\boldsymbol{u}_\star^n\|^2+\|\widetilde{\mathbf{u}}_{ch}^{n+1}-\boldsymbol{u}_\star^n\|^2)+\frac{\nu}{2}\Delta t\|\nabla\widetilde{\mathbf{u}}_{ch}^{n+1}\|^2-\Delta t(p_{ch}^n,\nabla\cdot\widetilde{\mathbf{u}}_{ch}^{n+1})\\ +\Delta t\langle 2p_{mh}^{n+1}-p_{mh}^n-p_{ch}^{n+1}+p_{ch}^n,\widetilde{\mathbf{u}}_{ch}^{n+1}\cdot\mathbf{n}_c\rangle\\ +\Delta t\frac{\alpha\nu\sqrt{\mathrm{d}}}{\sqrt{\mathrm{tr}(\chi)}}\langle P_\tau\widetilde{\mathbf{u}}_{ch}^{n+1},P_\tau\widetilde{\mathbf{u}}_{ch}^{n+1}\rangle\le 0.\end{aligned}\tag{76}$$

Now, we deal with the term $\Delta t(p_{ch}^n,\nabla\cdot\widetilde{\mathbf{u}}_{ch}^{n+1})$ in the above equation. We first take $q_h=\Delta t^2 p_{ch}^n$ in (58) and use (75) and (69) to obtain

$$\frac{1}{2}\Delta t^2(\|\nabla p_{ch}^{n+1}\|^2-\|\nabla p_{ch}^n\|^2-\|\nabla p_{ch}^{n+1}-\nabla p_{ch}^n\|^2)+\Delta t(\nabla\cdot\widetilde{\mathbf{u}}_{ch}^{n+1},p_{ch}^n)=0.\tag{77}$$

Taking $\boldsymbol{v}_h=-\Delta t(\boldsymbol{u}_{ch}^{n+1}-\widetilde{\mathbf{u}}_{ch}^{n+1})$ in (57) and applying (69), we have

$$-\|\boldsymbol{u}_{ch}^{n+1}-\widetilde{\mathbf{u}}_{ch}^{n+1}\|^2-\Delta t(\nabla p_{ch}^{n+1}-\nabla p_{ch}^n,\boldsymbol{u}_{ch}^{n+1}-\widetilde{\mathbf{u}}_{ch}^{n+1})=0.\tag{78}$$

Using Green's equation and the divergence-free conditions (67) and (69), we get

$$-\|\boldsymbol{u}_{ch}^{n+1}-\widetilde{\mathbf{u}}_{ch}^{n+1}\|^2-\Delta t(p_{ch}^{n+1}-p_{ch}^n,\nabla\cdot\widetilde{\mathbf{u}}_{ch}^{n+1})=0.\tag{79}$$

Taking $q_h=\Delta t^2(p_{ch}^{n+1}-p_{ch}^n)$ in (58), we have

$$\Delta t^2\|\nabla p_{ch}^{n+1}-\nabla p_{ch}^n\|^2+\Delta t(\nabla\cdot\widetilde{\mathbf{u}}_{ch}^{n+1},p_{ch}^{n+1}-p_{ch}^n)=0.\tag{80}$$

Adding (79) and (80) and multiplying $\frac{1}{2}$, we derive

$$\frac{1}{2}\Delta t^2\|\nabla p_{ch}^{n+1}-\nabla p_{ch}^n\|^2=\frac{1}{2}\|\boldsymbol{u}_{ch}^{n+1}-\widetilde{\mathbf{u}}_{ch}^{n+1}\|^2.\tag{81}$$

Taking $\boldsymbol{v}_h=\Delta t\boldsymbol{u}_{ch}^{n+1}$ in (57) and using the identity (75) and Green's theorem, we obtain

$$\frac{1}{2}[\|\boldsymbol{u}_{ch}^{n+1}\|^2-\|\widetilde{\mathbf{u}}_{ch}^{n+1}\|^2+\|\boldsymbol{u}_{ch}^{n+1}-\widetilde{\mathbf{u}}_{ch}^{n+1}\|^2]+\Delta t\langle p_{ch}^{n+1}-p_{ch}^n,\boldsymbol{u}_{ch}^{n+1}\cdot\mathbf{n}_c\rangle=0.\tag{82}$$

Taking the inner product of (73) with $\boldsymbol{u}_\star^n$ and using the identity (75), we obtain

$$\frac{1}{2}[\|\boldsymbol{u}_\star^n\|^2-\|\boldsymbol{u}_{ch}^n\|^2+\|\boldsymbol{u}_\star^n-\boldsymbol{u}_{ch}^n\|^2]=\Delta t(w_{ch}^{n+1}\nabla\phi_{ch}^n,\boldsymbol{u}_\star^n).\tag{83}$$

Adding (76), (77), (81), (82), and (83) and applying (69), we obtain

$$\begin{aligned}\frac{1}{2}[\|\boldsymbol{u}_{ch}^{n+1}\|^2-\|\boldsymbol{u}_{ch}^n\|^2+\|\widetilde{\mathbf{u}}_{ch}^{n+1}-\boldsymbol{u}_\star^n\|^2+\|\boldsymbol{u}_\star^n-\boldsymbol{u}_{ch}^n\|^2]\\ +\frac{1}{2}\Delta t^2(\|\nabla p_{ch}^{n+1}\|^2-\|\nabla p_{ch}^n\|^2)\\ +\frac{\nu}{2}\Delta t\|\nabla\widetilde{\mathbf{u}}_{ch}^{n+1}\|^2-\Delta t(w_{ch}^{n+1}\nabla\phi_{ch}^n,\boldsymbol{u}_\star^n)\\ +\Delta t\langle 2p_{mh}^{n+1}-p_{mh}^n,\boldsymbol{u}_{ch}^{n+1}\cdot\mathbf{n}_c,\rangle\\ +\Delta t\frac{\alpha\nu\sqrt{\mathrm{d}}}{\sqrt{\mathrm{tr}(\chi)}}\langle P_\tau\widetilde{\mathbf{u}}_{ch}^{n+1},P_\tau\widetilde{\mathbf{u}}_{ch}^{n+1}\rangle\le 0.\end{aligned}\tag{84}$$

Taking $\psi_h = \Delta t w_{ch}^{n+1}$ in (54), we get

$$\begin{aligned}(\phi_{ch}^{n+1} - \phi_{ch}^{n}, w_{ch}^{n+1}) + \Delta t(\boldsymbol{u}_\star^n \cdot \nabla \phi_{ch}^n, w_{ch}^{n+1}) + \Delta t M_c \|\nabla w_{ch}^{n+1}\|^2 \\ + \Delta t \langle M_m \nabla w_{mh}^n \cdot \mathbf{n}_m, w_{ch}^{n+1}\rangle = 0.\end{aligned} \tag{85}$$

Next, we take $\omega_h = -(\phi_{ch}^{n+1} - \phi_{ch}^n)$ in (55). Using the identity (75) and the Taylor expansion

$$F(\phi^{n+1}) - F(\phi^n) = f(\phi^n)(\phi^{n+1} - \phi^n) + \frac{F''(\xi^n)}{2}(\phi^{n+1} - \phi^n)^2, \tag{86}$$

we have

$$\begin{aligned}-(w_{ch}^{n+1}, \phi_{ch}^{n+1} - \phi_{ch}^n) + \frac{\gamma\epsilon}{2}[\|\nabla\phi_{ch}^{n+1}\|^2 - \|\nabla\phi_{ch}^n\|^2] + \gamma(F(\phi_{ch}^{n+1}) - F(\phi_{ch}^n), 1) \\ + \frac{\gamma}{\epsilon}\|\phi_{ch}^{n+1} - \phi_{ch}^n\|^2 + \frac{\gamma\epsilon}{2}\|\nabla\phi_{ch}^{n+1} - \nabla\phi_{ch}^n\|^2 \\ + \gamma\epsilon\langle\nabla\phi_{mh}^n \cdot \mathbf{n}_m, \phi_{ch}^{n+1} - \phi_{ch}^n\rangle \\ \le \frac{\gamma}{2}|F''(\xi^n)|\|\phi_{ch}^{n+1} - \phi_{ch}^n\|^2,\end{aligned} \tag{87}$$

and then, combining (42) and (87), we derive

$$\begin{aligned}-(w_{ch}^{n+1}, \phi_{ch}^{n+1} - \phi_{ch}^n) + \frac{\gamma\epsilon}{2}[\|\nabla\phi_{ch}^{n+1}\|^2 - \|\nabla\phi_{ch}^n\|^2] + \gamma(F(\phi_{ch}^{n+1}) - F(\phi_{ch}^n), 1) \\ + \frac{\gamma\epsilon}{2}\|\nabla\phi_{ch}^{n+1} - \nabla\phi_{ch}^n\|^2 \\ \le -\gamma\epsilon\langle\nabla\phi_{mh}^n \cdot \mathbf{n}_m, \phi_{ch}^{n+1} - \phi_{ch}^n\rangle.\end{aligned} \tag{88}$$

Adding (84), (85), and (88), we get

$$\begin{aligned}\frac{1}{2}[\|\boldsymbol{u}_{ch}^{n+1}\|^2 - \|\boldsymbol{u}_{ch}^n\|^2] + \frac{\gamma\epsilon}{2}[\|\nabla\phi_{ch}^{n+1}\|^2 - \|\nabla\phi_{ch}^n\|^2] + \gamma(F(\phi_{ch}^{n+1}) - F(\phi_{ch}^n), 1) \\ + \frac{1}{2}\Delta t^2(\|\nabla p_{ch}^{n+1}\|^2 - \|\nabla p_{ch}^n\|^2) + \frac{\nu}{2}\Delta t\|\nabla\widetilde{\mathbf{u}}_{ch}^{n+1}\|^2 + \Delta t M_c\|\nabla w_{ch}^{n+1}\|^2 \\ + \frac{\gamma\epsilon}{2}\|\nabla\phi_{ch}^{n+1} - \nabla\phi_{ch}^n\|^2 + \frac{1}{2}[\|\widetilde{\mathbf{u}}_{ch}^{n+1} - \boldsymbol{u}_\star^n\|^2 + \|\boldsymbol{u}_\star^n - \boldsymbol{u}_{ch}^n\|^2] \\ \le -\Delta t\frac{\alpha\nu\sqrt{\mathrm{d}}}{\sqrt{\mathrm{tr}(\chi)}}\langle P_\tau\widetilde{\mathbf{u}}_{ch}^{n+1}, P_\tau\widetilde{\mathbf{u}}_{ch}^{n+1}\rangle - \Delta t\langle 2p_{mh}^{n+1} - p_{mh}^n, \boldsymbol{u}_{ch}^{n+1} \cdot \mathbf{n}_c\rangle \\ - \Delta t\langle M_m\nabla w_{mh}^n \cdot \mathbf{n}_m, w_{ch}^{n+1}\rangle - \gamma\epsilon\langle\nabla\phi_{mh}^n \cdot \mathbf{n}_m, \phi_{ch}^{n+1} - \phi_{ch}^n\rangle.\end{aligned} \tag{89}$$

Next, we consider the matrix part. Choosing $\psi_h = \Delta t w_{mh}^{n+1}$ in (51) and using (59), we derive

$$\begin{aligned}(\phi_{mh}^{n+1} - \phi_{mh}^n, w_{mh}^{n+1}) = &-\Delta t(\boldsymbol{u}_{mh}^{n+1} \cdot \nabla\phi_{mh}^n, w_{mh}^{n+1}) \\ &- \Delta t M_m\|\nabla w_{mh}^{n+1}\|^2 - \Delta t\langle M_c\nabla w_{ch}^n \cdot \mathbf{n}_c, w_{mh}^{n+1}\rangle.\end{aligned} \tag{90}$$

Next, taking $\omega_h = -(\phi_{mh}^{n+1} - \phi_{mh}^n)$ in (52) and using (75), (86), and (42), we obtain

$$\begin{aligned}-(w_{mh}^{n+1}, \phi_{mh}^{n+1} - \phi_{mh}^n) + \frac{\gamma\epsilon}{2}[\|\nabla\phi_{mh}^{n+1}\|^2 - \|\nabla\phi_{mh}^n\|^2] + \gamma(F(\phi_{mh}^{n+1}) - F(\phi_{mh}^n), 1) \\ \le -\frac{\gamma\epsilon}{2}\|\nabla\phi_{mh}^{n+1} - \nabla\phi_{mh}^n\|^2 - \gamma\epsilon\langle\nabla\phi_{ch}^n \cdot \mathbf{n}_c, \phi_{mh}^{n+1} - \phi_{mh}^n\rangle.\end{aligned} \tag{91}$$

Now we take inner product of (59) with $\Delta t \boldsymbol{u}_{mh}^{n+1}$ to get

$$\Delta t k^{-1} \|\boldsymbol{u}_{mh}^{n+1}\|^2 = -\Delta t(\nabla p_{mh}^n, \boldsymbol{u}_{mh}^{n+1}) + \Delta t(w_{mh}^{n+1} \nabla \phi_{mh}^n, \boldsymbol{u}_{mh}^{n+1}). \tag{92}$$

From (59), (53) can be written as

$$-(\boldsymbol{u}_{mh}^{n+1}, \nabla q_h) + \mathbb{K}(\nabla p_{mh}^{n+1} - \nabla p_{mh}^n, \nabla q_h) - \langle \boldsymbol{u}_{ch}^n \cdot \mathbf{n}_c, q_h \rangle = 0. \tag{93}$$

We take $q_h = \Delta t p_{mh}^n$ in (93) and utilize the identity (75) to obtain

$$\begin{aligned} &- \Delta t(\boldsymbol{u}_{mh}^{n+1}, \nabla p_{mh}^n) + \frac{1}{2}\Delta t k[\|\nabla p_{mh}^{n+1}\|^2 - \|\nabla p_{mh}^n\|^2 \\ &- \|\nabla p_{mh}^{n+1} - \nabla p_{mh}^n\|^2] = \Delta t \langle \boldsymbol{u}_{ch}^n \cdot \mathbf{n}_c, p_{mh}^n \rangle. \end{aligned} \tag{94}$$

Taking the sum of (92) and (94), we get

$$\begin{aligned} \Delta t k^{-1} \|\boldsymbol{u}_{mh}^{n+1}\|^2 + \frac{1}{2}\Delta t k[\|\nabla p_{mh}^{n+1}\|^2 - \|\nabla p_{mh}^n\|^2 - \|\nabla p_{mh}^{n+1} - \nabla p_{mh}^n\|^2] \\ = \Delta t(w_{mh}^{n+1} \nabla \phi_{mh}^n, \boldsymbol{u}_{mh}^{n+1}) + \Delta t \langle \boldsymbol{u}_{ch}^n \cdot \mathbf{n}_c, p_{mh}^n \rangle. \end{aligned} \tag{95}$$

Now, we estimate the term $\|\nabla p_{mh}^{n+1} - \nabla p_{mh}^n\|^2$. From (60), we have

$$\|\widetilde{\mathbf{u}}_{mh}^{n+1} - \boldsymbol{u}_{mh}^{n+1}\|^2 = k^2 \|\nabla p_{mh}^{n+1} - \nabla p_{mh}^n\|^2. \tag{96}$$

Taking the inner product of (60) with $\mathbb{K}^{-1}\widetilde{\mathbf{u}}_{mh}^{n+1}$ and using (75), (61), (64), and (10), we obtain

$$\frac{1}{2}k^{-1}[\|\widetilde{\mathbf{u}}_{mh}^{n+1}\|^2 - \|\boldsymbol{u}_{mh}^{n+1}\|^2 + \|\widetilde{\mathbf{u}}_{mh}^{n+1} - \boldsymbol{u}_{mh}^{n+1}\|^2] = \langle \boldsymbol{u}_{ch}^{n+1} \cdot \mathbf{n}_c, p_{mh}^{n+1} - p_{mh}^n \rangle. \tag{97}$$

Multiplying (96) by $-\frac{1}{2}\Delta t k^{-1}$, multiplying (97) by Δt, and then adding them to (95), we obtain

$$\begin{aligned} &\frac{1}{2}\Delta t k^{-1}[\|\boldsymbol{u}_{mh}^{n+1}\|^2 + \|\widetilde{\mathbf{u}}_{mh}^{n+1}\|^2] + \frac{1}{2}\Delta t k[\|\nabla p_{mh}^{n+1}\|^2 - \|\nabla p_{mh}^n\|^2] \\ &\qquad = \Delta t(w_{mh}^{n+1} \nabla \phi_{mh}^n, \boldsymbol{u}_{mh}^{n+1}) + \Delta t \langle \boldsymbol{u}_{ch}^n \cdot \mathbf{n}_c, p_{mh}^n \rangle \\ &\qquad + \Delta t \langle \boldsymbol{u}_{ch}^{n+1} \cdot \mathbf{n}_c, p_{mh}^{n+1} - p_{mh}^n \rangle. \end{aligned} \tag{98}$$

Adding (90), (91), and (98), we obtain

$$\begin{aligned} &\frac{1}{2}\gamma\epsilon[\|\nabla \phi_{mh}^{n+1}\|^2 - \|\nabla \phi_{mh}^n\|^2] \\ &\qquad + \gamma(F(\phi_{mh}^{n+1}) - F(\phi_{mh}^n), 1) \\ &\qquad + \frac{1}{2}\Delta t k[\|\nabla p_{mh}^{n+1}\|^2 - \|\nabla p_{mh}^n\|^2] \\ &\qquad \le -\frac{1}{2}\Delta t k^{-1}[\|\boldsymbol{u}_{mh}^{n+1}\|^2 + \|\widetilde{\mathbf{u}}_{mh}^{n+1}\|^2] - \frac{1}{2}\gamma\epsilon\|\nabla \phi_{mh}^{n+1} - \nabla \phi_{mh}^n\|^2 \\ &\qquad - \Delta t M_m \|\nabla w_{mh}^{n+1}\|^2 + \Delta t \langle \boldsymbol{u}_{ch}^n \cdot \mathbf{n}_c, p_{mh}^n \rangle \\ &\qquad - \Delta t \langle M_c \nabla w_{ch}^n \cdot \mathbf{n}_c, w_{mh}^{n+1} \rangle \\ &\qquad - \gamma\epsilon \langle \nabla \phi_{ch}^n \cdot \mathbf{n}_c, \phi_{mh}^{n+1} - \phi_{mh}^n \rangle + \Delta t \langle \boldsymbol{u}_{ch}^{n+1} \cdot \mathbf{n}_c, p_{mh}^{n+1} - p_{mh}^n \rangle. \end{aligned} \tag{99}$$

Adding (89) and (99) together and applying the interface conditions (13)–(16), we obtain

$$\begin{aligned}
&\frac{1}{2}[\|\boldsymbol{u}_{ch}^{n+1}\|^2 - \|\boldsymbol{u}_{ch}^{n}\|^2] + \frac{\gamma\epsilon}{2}[\|\nabla\phi_{ch}^{n+1}\|^2 \\
&\qquad - \|\nabla\phi_{ch}^{n}\|^2] + \gamma(F(\phi_{ch}^{n+1}) - F(\phi_{ch}^{n}), 1) \\
&\qquad + \frac{1}{2}\gamma\epsilon[\|\nabla\phi_{mh}^{n+1}\|^2 - \|\nabla\phi_{mh}^{n}\|^2] + \gamma(F(\phi_{mh}^{n+1}) - F(\phi_{mh}^{n}), 1) \\
&\qquad + \frac{1}{2}\Delta t^2(\|\nabla p_{ch}^{n+1}\|^2 - \|\nabla p_{ch}^{n}\|^2) \\
&\qquad + \frac{1}{2}\Delta tk[\|\nabla p_{mh}^{n+1}\|^2 - \|\nabla p_{mh}^{n}\|^2] + \Delta t\langle \boldsymbol{u}_{ch}^{n+1}\cdot\mathbf{n}_c, p_{mh}^{n+1}\rangle \\
&\qquad - \Delta t\langle \boldsymbol{u}_{ch}^{n}\cdot\mathbf{n}_c, p_{mh}^{n}\rangle \le -\frac{1}{2}[\|\widetilde{\mathbf{u}}_{ch}^{n+1} - \boldsymbol{u}_{\star}^{n}\|^2 + \|\boldsymbol{u}_{\star}^{n} - \boldsymbol{u}_{ch}^{n}\|^2] \\
&\qquad - \frac{\nu}{2}\Delta t\|\nabla\widetilde{\mathbf{u}}_{ch}^{n+1}\|^2 - \frac{1}{2}\gamma\epsilon\|\nabla\phi_{mh}^{n+1} - \nabla\phi_{mh}^{n}\|^2 \\
&\qquad - \Delta tM_c\|\nabla w_{ch}^{n+1}\|^2 - \Delta tM_m\|\nabla w_{mh}^{n+1}\|^2 - \frac{\gamma\epsilon}{2}\|\nabla\phi_{ch}^{n+1} - \nabla\phi_{ch}^{n}\|^2 \\
&\qquad - \frac{1}{2}\Delta tk^{-1}[\|\boldsymbol{u}_{mh}^{n+1}\|^2 + \|\widetilde{\mathbf{u}}_{mh}^{n+1}\|^2] - \Delta t\frac{\alpha\nu\sqrt{\mathrm{d}}}{\sqrt{\mathrm{tr}(\chi)}}\langle P_\tau\widetilde{\mathbf{u}}_{ch}^{n+1}, P_\tau\widetilde{\mathbf{u}}_{ch}^{n+1}\rangle,
\end{aligned}$$

which completes the proof of (70).

Now we prove the energy stability. Using Lemma 1 in [22] and (67), we obtain

$$\begin{aligned}
\Delta t|\langle \boldsymbol{u}_{ch}^{n+1}\cdot\mathbf{n}_c, p_{mh}^{n+1}\rangle| &\le C\Delta t\|\boldsymbol{u}_{ch}^{n+1}\|\|\nabla p_{mh}^{n+1}\| \\
&\le \frac{1}{4}\|\boldsymbol{u}_{ch}^{n+1}\|^2 + C^2\Delta t^2\|\nabla p_{mh}^{n+1}\|^2. \qquad (100)
\end{aligned}$$

Based on $\mathcal{D}^{n+1} \ge 0$, (100), and (72), the inequality (70) leads to

$$\begin{aligned}
&E^0 + \frac{1}{2}\Delta t^2\|\nabla p_{ch}^{0}\|^2 \\
&\quad + \frac{1}{2}\Delta tk\|\nabla p_{mh}^{0}\|^2 + \Delta t\langle \boldsymbol{u}_{ch}^{0}\cdot\mathbf{n}_c, p_{mh}^{0}\rangle \\
&\quad \ge E^n + \frac{1}{2}\Delta t^2\|\nabla p_{ch}^{n}\|^2 + \frac{1}{2}\Delta tk\|\nabla p_{mh}^{n}\|^2 + \Delta t\langle \boldsymbol{u}_{ch}^{n}\cdot\mathbf{n}_c, p_{mh}^{n}\rangle \\
&\quad \ge E^{n+1} + \frac{1}{2}\Delta t^2\|\nabla p_{ch}^{n+1}\|^2 + \frac{1}{2}\Delta tk\|\nabla p_{mh}^{n+1}\|^2 + \Delta t\langle \boldsymbol{u}_{ch}^{n+1}\cdot\mathbf{n}_c, p_{mh}^{n+1}\rangle \\
&\quad \ge E^{n+1} + \frac{1}{2}\Delta t^2\|\nabla p_{ch}^{n+1}\|^2 + \frac{1}{2}\Delta tk\|\nabla p_{mh}^{n+1}\|^2 \\
&\quad - \int_{\Omega_c}\frac{1}{4}|\boldsymbol{u}_{ch}^{n+1}|^2 d\boldsymbol{x} - C^2\Delta t^2\|\nabla p_{mh}^{n+1}\|^2 \\
&\quad \ge \int_{\Omega_c}\frac{1}{4}|\boldsymbol{u}_{ch}^{n+1}|^2 d\boldsymbol{x} + \gamma\int_{\Omega_c}\left[\frac{\epsilon}{2}|\nabla\phi_{ch}^{n}|^2 + F(\phi_{ch}^{n})\right]d\boldsymbol{x} \\
&\quad + \gamma\int_{\Omega_m}\left[\frac{\epsilon}{2}|\nabla\phi_{mh}^{n}|^2 + F(\phi_{mh}^{n})\right]d\boldsymbol{x} + \frac{1}{2}\Delta t^2\|\nabla p_{ch}^{n+1}\|^2 \\
&\quad + \left(\frac{1}{2}\Delta tk - C^2\Delta t^2\right)\|\nabla p_{mh}^{n+1}\|^2 \ge 0 \qquad (101)
\end{aligned}$$

if the constraint (74) is satisfied. This leads to the energy stability of the numerical scheme (51)–(58) and completes the proof of Theorem 3.6. ∎

4. Numerical example. In this section, we present various 2D numerical examples to illustrate the features of the proposed model and numerical methods. The first example is provided to show the convergence and accuracy. The second example is to verify that the proposed method obeys the energy dissipation as presented in Theorem 3.6. The third test illustrates the shape evolvement of a droplet passing through the interface driven by boundary-injection. The last experiment is the simulation for a conduit coupled with two types of porous media: single crack medium and heterogeneous medium.

Example 1: Convergence and accuracy. Consider the model problem on $\Omega = [0,1] \times [0,2]$ where $\Omega_m = [0,1] \times [0,1]$ and $\Omega_c = [0,1] \times [1,2]$. Set $M_m = 1$, $\gamma = 1$, $\epsilon = 1$, $\nu = 1$, $M_c = 1$, and $\mathbb{K} = \mathbb{I}$. The boundary condition functions and the source terms are chosen such that the following functions are the exact solutions:

$$\begin{cases} p_m = \phi_m = w_m = g(x)g_m(y)\cos(\pi t), \\ \boldsymbol{u}_c = [x^2(y-1)^2, \ -\frac{2}{3}x(y-1)^3]^T \cos(\pi t), \\ p_c = \phi_c = w_c = g(x)g_c(y)\cos(\pi t), \end{cases} \tag{102}$$

where $g(x) = 16x^2(x-1)^2, g_m(y) = 16y^2(y-1)^2, g_c(y) = 16(y-1)^2(y-2)^2$. All the numerical results below are for $T = 1$. For the Navier–Stokes equation, we consider the Taylor–Hood elements. For the Darcy equation and the second order mixed formulation of the Cahn–Hilliard equation, we consider the linear or quadratic elements. That is, for $p_m - \phi_m - w_m - \boldsymbol{u}_c - p_c - \phi_c - w_c$, we consider two different types of finite elements: $P_1 - P_1 - P_1 - \mathbf{P}_2 - P_1 - P_1 - P_1$ elements and $P_2 - P_2 - P_2 - \mathbf{P}_2 - P_1 - P_2 - P_2$ elements. The L^2, L^∞, and H^1 norm errors of the two types of finite elements are presented in Tables 2–3, respectively. The numerical results in the two tables clearly show the optimal convergence rates of the two types of finite elements in all of the L^2, L^∞, and H^1 norms. In the following three numerical examples, we only consider the $P_2 - P_2 - P_2 - \mathbf{P}_2 - P_1 - P_2 - P_2$ finite elements.

Example 2: Shape relaxation and energy dissipation. We simulate the evolution of a square shaped bubble in the domain $\Omega = [0,1] \times [0,2]$, where $\Omega_m = [0,1] \times [0,1]$ and $\Omega_c = [0,1] \times [1,2]$. We choose $M_m = 0.1$, $\gamma = 0.1$, $\epsilon = 0.01$, $\nu = 1$, $M_c = 1$, and $\mathbb{K} = 0.1\mathbb{I}$. The initial velocity, pressure, and chemical potential are set to zero. Figure 2 shows the dynamics evolution of the bubble which turns into a circle under the effect of surface tension. The relative discrete total energy E^n/E^0 is presented in Figure 3. We can see that the discrete energy of the numerical solution indeed decays with time, which agrees with the theoretical result in Theorem 3.6 and validates the interface conditions (13)–(16).

Example 3: Boundary-driven flow. In this experiment, we simulate a droplet passing through the interface driven by boundary-injection [19, 48]. Consider the model problem on $\Omega = [0,2] \times [0,1]$ where $\Omega_m = [1,2] \times [0,1]$ and $\Omega_c = [0,1] \times [0,1]$. We choose $M_m = 0.01$, $\gamma = 0.001$, $\epsilon = 0.01$, $\nu = 0.1$, $M_c = 0.01$, and $\mathbb{K} = 0.01\mathbb{I}$. The parabolic velocity is imposed on the left boundary, i.e., $\boldsymbol{u}_c = -4y(y-1)$ on $\Gamma_{in} := \{0\} \times [0,1]$ in Ω_c. Ambient pressure is assigned to zero for the CHD pressure, i.e., $p_m = 0$ on $\Gamma_{out} := \{2\} \times [0,1]$. A droplet of nonwetting phase is put in the free-flow region Ω_c initially at

$$\phi_m^0(x,y) = -\tanh\left((0.15 - \sqrt{(x-0.3)^2 + (y-0.5)^2})/(\sqrt{2}\epsilon)\right). \tag{103}$$

A uniform mesh with the step size $h = \frac{1}{32}$ and a uniform time partition with the time

TABLE 2
The order of convergence for error norms with $\Delta t = 0.01h$ at time $T = 1$ by $P_1 - P_1 - P_1 - \mathbf{P}_2 - P_1 - P_1 - P_1$ element.

	h	L^2	Order	L^∞	Order	H^1	Order
p_m	1/8	2.9388E-02		8.6492E-02		5.6065E-01	
	1/16	7.7769E-03	1.9180	2.3405E-02	1.8858	2.8885E-01	0.95680
	1/32	1.9732E-03	1.9786	5.9710E-03	1.9708	1.4551E-01	0.98906
	1/64	4.9516E-04	1.9946	1.5004E-03	1.9927	7.2901E-02	0.99725
ϕ_m	1/8	2.6004E-02		7.1988E-02		5.5962E-01	
	1/16	6.8771E-03	1.9189	1.8829E-02	1.9348	2.8871E-01	0.95485
	1/32	1.7445E-03	1.9790	4.7591E-03	1.9842	1.4550E-01	0.98853
	1/64	4.3774E-04	1.9947	1.1930E-03	1.9961	7.2898E-02	0.99712
w_m	1/8	2.3283E-02		5.3784E-02		5.6327E-01	
	1/16	6.1867E-03	1.9120	1.4246E-02	1.9166	2.8919E-01	0.96184
	1/32	1.5706E-03	1.9779	3.7209E-03	1.9368	1.4557E-01	0.99032
	1/64	3.9416E-04	1.9945	9.5222E-04	1.9663	7.2906E-02	0.99757
$\boldsymbol{u}_c$	1/8	2.6838E-04		6.5960E-04		6.4452E-03	
	1/16	3.9594E-05	2.7609	9.9500E-05	2.7288	1.3429E-03	2.2628
	1/32	6.0249E-06	2.7163	1.3981E-05	2.8312	2.9941E-04	2.1652
	1/64	8.7062E-07	2.7908	1.8850E-06	2.8909	6.9915E-05	2.0984
p_c	1/8	2.1920E-02		4.9205E-02		5.7781E-01	
	1/16	5.7452E-03	1.9318	1.2948E-02	1.9261	2.9238E-01	0.98273
	1/32	1.4485E-03	1.9878	3.3563E-03	1.9478	1.4622E-01	0.99972
	1/64	3.6125E-04	2.0035	8.5117E-04	1.9793	7.3054E-02	1.0011
ϕ_c	1/8	2.6328E-02		7.3112E-02		5.5961E-01	
	1/16	6.9616E-03	1.9191	1.9135E-02	1.9339	2.8870E-01	0.95484
	1/32	1.7658E-03	1.9791	4.8373E-03	1.9840	1.4551E-01	0.98852
	1/64	4.4308E-04	1.9947	1.2127E-03	1.9960	7.2898E-02	0.99712
w_c	1/8	2.6222E-02		7.3129E-02		5.5962E-01	
	1/16	6.9308E-03	1.9197	1.9191E-02	1.9300	2.8871E-01	0.95484
	1/32	1.7577E-03	1.9793	4.8555E-03	1.9828	1.4551E-01	0.98853
	1/64	4.4100E-04	1.9948	1.2174E-03	1.9958	7.2898E-02	0.99712

step size $\Delta t = 0.001$ are used in this simulation. Figure 4 shows several snapshots of the droplet passing through the interface Γ under the influence of boundary-driven flow. Similar to the results in [49], we can observe that the front of the round droplet becomes a shape with two flat sides due to the parabolic velocity on the whole left boundary and takes the maximum value at the center line as shown in Figures 4(b)–4(c). The magnitude of the velocity in porous media is significantly smaller than that in conduit, which leads to the phenomenon that the front of the droplet becomes flatter and elongates in the vertical direction when it crosses the interface as presented in Figure 4(d), so that the volume of the droplet is preserved. The shape of the droplet becomes steady when it leaves the interface and completely enters the porous media as shown in Figures 4(e)–4(f). All of these reasonable observations validate the interface conditions, the model, and the numerical method proposed in this article.

Example 4: Effect of the hydraulic conductivity tensor of porous media. In the CHNSD model, we consider a heterogeneous, isotropic porous medium with hydraulic conductivity tensor $\mathbb{K}$ defined as [25]

$$\mathbb{K}(x, y) = k(x, y) \cdot \mathbb{I},$$

where $k(x, y)$ is a scalar depending on position (x, y), and $\mathbb{I}$ isthe unit tensor. In the

TABLE 3
The order of convergence for error norms with $\Delta t = 0.01h$ at time $T = 1$ by $P_2 - P_2 - P_2 - \mathbf{P}_2 - P_1 - P_2 - P_2$ element.

	h	L^2	Order	L^∞	Order	H^1	Order
p_m	1/8	1.3555E-03		3.9842E-03		8.3186E-02	
	1/16	1.6938E-04	3.0005	5.2751E-04	2.9170	2.1370E-02	1.9608
	1/32	2.1170E-05	3.0002	6.9320E-05	2.9278	5.3810E-03	1.9896
	1/64	2.6460E-06	3.0001	8.9229E-06	2.9577	1.3478E-03	1.9973
ϕ_m	1/8	1.3487E-03		4.1045E-03		8.3083E-02	
	1/16	1.6923E-04	2.9944	5.3183E-04	2.9482	2.1362E-02	1.9595
	1/32	2.1164E-05	2.9993	6.9486E-05	2.9362	5.3805E-03	1.9892
	1/64	2.6458E-06	2.9998	8.9281E-06	2.9603	1.3477E-03	1.9972
w_m	1/8	1.3732E-03		4.2575E-03		8.3140E-02	
	1/16	1.6992E-04	3.0146	5.3646E-04	2.9885	2.1365E-02	1.9603
	1/32	2.1187E-05	3.0036	6.9623E-05	2.9458	5.3807E-03	1.9894
	1/64	2.6466E-06	3.0010	8.9281E-06	2.9625	1.3477E-03	1.9973
$\boldsymbol{u}_c$	1/8	2.7395E-04		6.5801E-04		7.2584E-03	
	1/16	3.9468E-05	2.7952	9.6047E-05	2.7763	1.4040E-03	2.3696
	1/32	5.9881E-06	2.7205	1.3572E-05	2.8231	3.0371E-04	2.2088
	1/64	8.6258E-07	2.7954	1.8370E-06	2.8852	7.0195E-05	2.1133
p_c	1/8	2.3596E-02		4.9812E-02		5.9412E-01	
	1/16	6.1636E-03	1.9367	1.2667E-02	1.9641	2.9429E-01	1.0135
	1/32	1.5527E-03	1.9890	3.1969E-03	1.9977	1.4645E-01	1.0068
	1/64	3.8613E-04	2.0076	7.9502E-04	2.0076	7.3083E-02	1.0028
ϕ_c	1/8	1.3485E-03		4.1042E-03		8.3083E-02	
	1/16	1.6924E-04	2.9943	5.3182E-04	2.9481	2.1362E-02	1.9595
	1/32	2.1165E-05	2.9993	6.9486E-05	2.9362	5.3805E-03	1.9892
	1/64	2.6459E-06	2.9998	8.9281E-06	2.9603	1.3477E-03	1.9972
w_c	1/8	1.3467E-03		4.1057E-03		8.3083E-02	
	1/16	1.6919E-04	2.9928	5.3188E-04	2.9485	2.1362E-02	1.9595
	1/32	2.1163E-05	2.9990	6.9518E-05	2.9357	5.3805E-03	1.9892
	1/64	2.6458E-06	2.9998	8.9282E-06	2.9609	1.3477E-03	1.9972

first case, we consider a single crack along a sine curve with

$$k(x,y) = \max\left\{\exp\left(-\left(\frac{y-0.5-0.1\sin(5x-5)}{0.1}\right)^2\right), 0.01\right\}. \tag{104}$$

The hydraulic conductivity field for this case is shown in Figure 5(a).

Choose the computational domain $\Omega = [0,3] \times [0,1]$ where $\Omega_m = [1,3] \times [0,1]$, $\Omega_c = [0,1] \times [0,1]$, and $\Gamma = \{1\} \times [0,1]$. Other parameters used in this simulation are the same as those in Example 3. Figure 6 shows the evolution of saturation distribution for the above single crack medium at different time. When the droplet moves into the porous media through the interface, its location is right around the left end of the crack. Since the permeability is much higher in the crack, the droplet slowly meanders its way along the crack and deforms into a shape similar to the crack.

If the location of the single crack is lower as illustrated in Figure 5(b), namely,

$$k(x,y) = \max\left\{\exp\left(-\left(\frac{y-0.3-0.1\sin(5x-5)}{0.1}\right)^2\right), 0.01\right\}, \tag{105}$$

then it is expected that the droplet will still be attracted by the crack. As the round droplet moves in the conduit domain, its front forms into an inclined corner. When the droplet passes through the interface, the droplet moves down and changes its

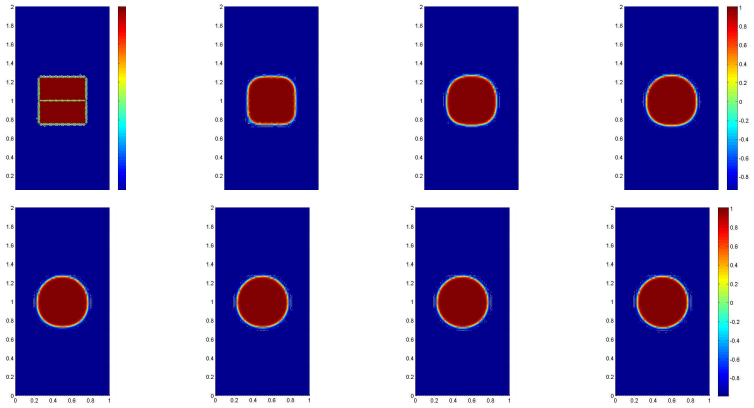

FIG. 2. *The dynamics of a square shaped bubble with* $h = \frac{1}{32}, \Delta t = 0.001$. *All the subfigures are indexed from left to right row by row as follows:* (a) $t = 0$, (b) $t = 0.05$, (c) $t = 0.1$, (d) $t = 0.15$, (e) $t = 0.2$, (f) $t = 0.3$, (g) $t = 0.5$, *and* (h) $t = 1.0$.

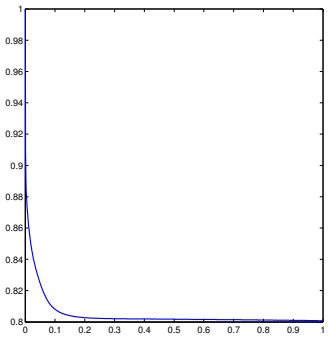

FIG. 3. *Energy plot* $h = \frac{1}{32}, \Delta t = 0.001$.

shape toward the crack. Then it again slowly meanders its way along the crack and deforms into a shape similar to the crack.

In Figures 6 and 7, one can see that the droplet is attracted toward the area with large hydraulic conductivity even before the droplet touches the interface. This clearly illustrates the effect of the hydraulic conductivity of the porous media domain on the free-flow domain through the physical interface conditions. As the droplet moves across the interface, the smooth and expected shape change of the droplet further validates the physically faithful interface conditions.

In the second case, we consider a porous medium with the following random hydraulic conductivity:

$$k(x,y) = \min\left\{\max\left\{\sum_{l=1}^{N}\Psi(x,y), 0.01\right\}, 4\right\}, \tag{106}$$

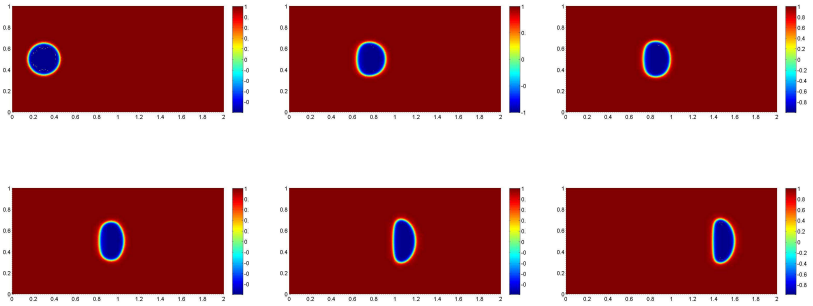

FIG. 4. *The dynamics of a droplet* $\mathbb{K} = 10^{-2}\mathbb{I}$ *with initial mesh* $h = \frac{1}{32}$ *and* $\Delta t = 0.001$. *All of the subfigures are indexed from left to right row by row as follows:* (a) $t = 0$, (b) $t = 0.5$, (c) $t = 0.6$, (d) $t = 0.7$, (e) $t = 0.9$, *and* (f) $t = 1.5$.

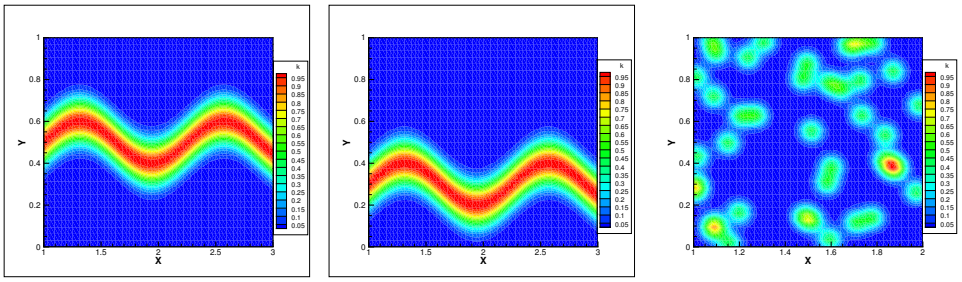

(a) Single crack medium (b) Single crack medium (c) Random medium

FIG. 5. *Permeability fields for a single crack medium (left, middle) and a random medium (right). (Figure is in color online.)*

where

$$\Psi(x,y) = \exp\left(-\left(\frac{x-1-x_l}{0.05}\right)^2 - \left(\frac{y-y_l}{0.05}\right)^2\right),$$

and the centers (x_l, y_l) are N randomly chosen locations inside the domain. This function models a domain in which there are $N = 40$ centers of higher permeability, representing regions with cracks embedded in a matrix of intact background rock.

Choose the computational domain $\Omega = [0,2] \times [0,1]$ where $\Omega_m = [1,2] \times [0,1]$, $\Omega_c = [0,1] \times [0,1]$, and $\Gamma = \{1\} \times [0,1]$. We use the same parameters as the first case in this example. Figure 5(c) shows one sample of the random medium. Figure 8 shows that the more mobile displacing fluid seeks pathways formed by the fractures and faults.

Before the droplet starts to cross the interface $\{1\} \times [0,1]$, Figure 8(c) shows that the front of the droplet starts to form two corners due to the interface conditions and the high permeability in two green areas centered around points $(1.08, 0.75)$ and $(1.15, 0.48)$ in Figure 5(c). And Figure 4(e) clearly shows the two corners caused by the effect of these two green areas of high permeability. When the droplet gets closer to the larger green area centered around the point $(1.23, 0.63)$ in Figure 5(c), the two

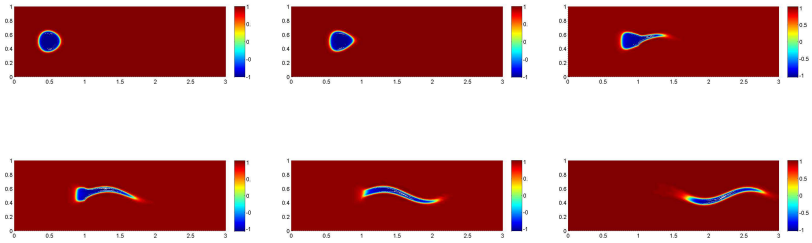

FIG. 6. *The dynamics of a droplet in the first single crack medium with initial mesh* $h = \frac{1}{32}$ *and* $\Delta t = 0.001$. *All the subfigures are indexed from left to right row by row as follows:* (a) $t = 0.2$, (c) $t = 0.4$, (e) $t = 0.6$, (f) $t = 0.7$, (g) $t = 0.8$, *and* (i) $t = 1.0$.

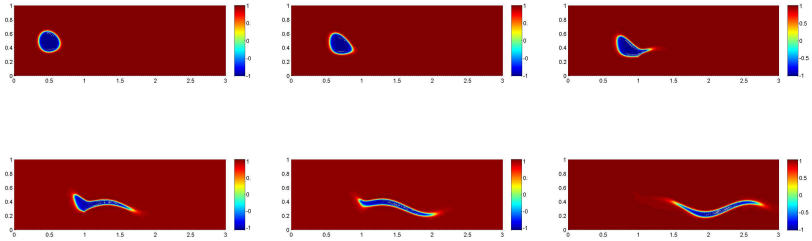

FIG. 7. *The dynamics of a droplet in the second single crack medium with initial mesh* $h = \frac{1}{32}$ *and* $\Delta t = 0.001$. *All the subfigures are indexed from left to right row by row as follows:* (a) $t = 0.2$, (b) $t = 0.4$, (c) $t = 0.55$, (d) $t = 0.7$, (e) $t = 0.8$, *and* (f) $t = 1.0$.

corners gradually become like fingers and move closer to each other because of the high permeability between them; see Figures 8(e) and 8(f). Then, more fingers are gradually formed in Figures 8(g)–8(i) due to the green areas with higher permeability around the middle part of Figure 5(c). Finally, when the droplet moves closer to the red area with the highest permeability, which is centered around point $(1.87, 0.37)$ in Figure 5(c), one finger of the droplet becomes larger than the others in Figures 8(h)–8(i) since more fluid tries to go through that area of the highest permeability. As presented in Figure 8, the evolution of the droplet verifies rationality of the seven interface conditions (10)–(16) and the CHNSD model again. The fingers we observe in this simulation is a phenomenon frequently found in both oil reservoirs and porous diffusion media of fuel cells [69].

5. Conclusions. In this paper, a decoupled, linearized, and energy stable finite element method is proposed to solve a time-dependent CHNSD model. The seven interface conditions are utilized to decouple the CHNS equation and the CHD equation. A linearization is utilized to deal with the nonlinearity of the two decoupled equation. A stabilization and another appropriate treatment of the interface terms is utilized to achieve the energy stability. Moreover, the energy law is analyzed for the model and a discrete energy stability is analyzed for the proposed numerical method. The features of the proposed method, such as the accuracy, energy dissipation, and applicability, are demonstrated by the numerical experiments.

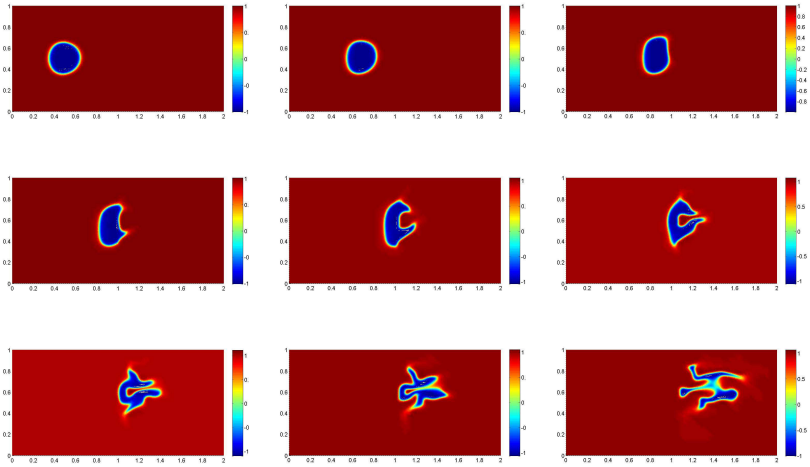

FIG. 8. *The dynamics of a droplet in random medium with initial mesh* $h = \frac{1}{32}$ *and* $\Delta t = 0.001$. *All the subfigures are indexed from left to right row by row as follows:* (a) $t = 0.2$, (b) $t = 0.4$, (c) $t = 0.6$, (d) $t = 0.7$, (e) $t = 0.8$, (f) $t = 0.9$, (g) $t = 1.0$, (h) $t = 1.1$, *and* (i) $t = 1.3$. *(Figure is in color online.)*

Acknowledgment. The authors thank Xiaoming Wang and Daozhi Han for some insights into the problem and many helpful discussions.

REFERENCES

[1] D. M. Anderson, G. B. McFadden, and A. A. Wheeler, *Diffuse-interface methods in fluid mechanics*, Annu. Rev. Fluid Mech., 30 (1998), pp. 139–165.

[2] T. Arbogast and D. S. Brunson, *A computational method for approximating a Darcy-Stokes system governing a vuggy porous medium*, Comput. Geosci., 11 (2007), pp. 207–218.

[3] T. Arbogast and H. L. Lehr, *Homogenization of a Darcy-Stokes system modeling vuggy porous media*, Comput. Geosci., 10 (2006), pp. 291–302.

[4] I. Babuška and G. N. Gatica, *A residual-based a posteriori error estimator for the Stokes–Darcy coupled problem*, SIAM J. Numer. Anal., 48 (2010), pp. 498–523, https://doi.org/10.1137/080727646.

[5] G. Beavers and D. Joseph, *Boundary conditions at a naturally permeable wall*, J. Fluid Mech., 30 (1967), pp. 197–207.

[6] Y. Boubendir and S. Tlupova, *Stokes-Darcy boundary integral solutions using preconditioners*, J. Comput. Phys., 228 (2009), pp. 8627–8641.

[7] Y. Boubendir and S. Tlupova, *Domain decomposition methods for solving Stokes–Darcy problems with boundary integrals*, SIAM J. Sci. Comput., 35 (2013), pp. B82–B106, https://doi.org/10.1137/110838376.

[8] L. A. Caffarelli and N. E. Muler, *An* L^∞ *bound for solutions of the Cahn-Hilliard equation*, Arch. Rational Mech. Anal., 133 (1995), pp. 129–144.

[9] J. W. Cahn and J. E. Hilliard, *Free energy of a nonuniform system.* I. *Interfacial free energy*, J. Chem. Phys., 28 (1958), pp. 258–267.

[10] M. Cai and M. Mu, *A multilevel decoupled method for a mixed Stokes/Darcy model*, J. Comput. Appl. Math., 236 (2012), pp. 2452–2465.

[11] M. Cai, M. Mu, and J. Xu, *Numerical solution to a mixed Navier-Stokes/Darcy model by the two-grid approach*, SIAM J. Numer. Anal., 47 (2009), pp. 3325–3338, https://doi.org/10.1137/080721868.

[12] J. Camano, G. N. Gatica, R. Oyarzua, R. Ruiz-Baier, and P. Venegas, *New fully-mixed finite element methods for the Stokes-Darcy coupling*, Comput. Methods Appl. Mech. Engrg., 295 (2015), pp. 362–395.

[13] Y. Cao, Y. Chu, X.-M. He, and M. Wei, *Decoupling the stationary Navier-Stokes-Darcy system with the Beavers-Joseph-Saffman interface condition*, Abstr. Appl. Anal., (2013), 136483.
[14] Y. Cao, M. Gunzburger, X.-M. He, and X. Wang, *Robin-Robin domain decomposition methods for the steady Stokes-Darcy model with Beaver-Joseph interface condition*, Numer. Math., 117 (2011), pp. 601–629.
[15] Y. Cao, M. Gunzburger, X.-M. He, and X. Wang, *Parallel, non-iterative, multi-physics domain decomposition methods for time-dependent Stokes-Darcy systems*, Math. Comp., 83 (2014), pp. 1617–1644.
[16] Y. Cao, M. Gunzburger, X. Hu, F. Hua, X. Wang, and W. Zhao, *Finite element approximation for Stokes–Darcy flow with Beavers–Joseph interface conditions*, SIAM. J. Numer. Anal., 47 (2010), pp. 4239–4256, https://doi.org/10.1137/080731542.
[17] A. Çeşmelioğlu, V. Girault, and B. Rivière, *Time-dependent coupling of Navier-Stokes and Darcy flows*, ESAIM Math. Model. Numer. Anal., 47 (2013), pp. 539–554.
[18] A. Çeşmelioğlu and B. Rivière, *Primal discontinuous Galerkin methods for time-dependent coupled surface and subsurface flow*, J. Sci. Comput., 40 (2009), pp. 115–140.
[19] J. Chen, S. Sun, and X. Wang, *A numerical method for a model of two-phase flow in a coupled free flow and porous media system*, J. Comput. Phys., 268 (2014), pp. 1–16.
[20] R. Chen, G. Ji, X. Yang, and H. Zhang, *Decoupled energy stable schemes for phase-field vesicle membrane model*, J. Comput. Phys., 302 (2015), pp. 509–523.
[21] W. Chen, M. Gunzburger, F. Hua, and X. Wang, *A parallel Robin–Robin domain decomposition method for the Stokes–Darcy system*, SIAM. J. Numer. Anal., 49 (2011), pp. 1064–1084, https://doi.org/10.1137/080740556.
[22] W. Chen, D. Han, and X. Wang, *Uniquely solvable and energy stable decoupled numerical schemes for the Cahn-Hilliard-Stokes-Darcy system for two-phase flows in karstic geometry*, Numer. Math., 137 (2017), pp. 229–255.
[23] Y. J. Choi and P. D. Anderson, *Cahn-Hilliard modeling of particles suspended in two-phase flows*, Int. J. Numer. Meth. Fluids, 69 (2012), pp. 995–1015.
[24] A. Christlieb, J. Jones, K. Promislow, B. Wetton, and M. Willoughby, *High accuracy solutions to energy gradient flows from material science models*, J. Chem. Phys., 257 (2014), pp. 192–215.
[25] C. C. Chueha, M. Secanella, W. Bangerthb, and N. Djilali, *Multi-level adaptive simulation of transient two-phase flow in heterogeneous porous media*, Comput Fluids, 39 (2010), pp. 1585–1596.
[26] N. Condette, C. Melcher, and E. Süli, *Spectral approximation of pattern-forming nonlinear evolution equations with double-well potentials of quadratic growth*, Math. Comp., 80 (2011), pp. 205–223.
[27] C. D'Angelo and P. Zunino, *Robust numerical approximation of coupled Stokes' and Darcy's flows applied to vascular hemodynamics and biochemical transport*, ESAIM Math. Model. Numer. Anal., 45 (2011), pp. 447–476.
[28] A. E. Diegel, X. Feng, and S. M. Wise, *Analysis of a mixed finite element method for a Cahn–Hilliard–Darcy–Stokes system*, SIAM J. Numer. Anal., 53 (2015), pp. 127–152, https://doi.org/10.1137/130950628.
[29] M. Discacciati, *Domain Decomposition Methods for the Coupling of Surface and Groundwater Flows*, Ph.D. thesis, Ecole Polytechnique Fédérale de Lausanne, Switzerland, 2004.
[30] M. Discacciati, E. Miglio, and A. Quarteroni, *Mathematical and numerical models for coupling surface and groundwater flows*, Appl. Numer. Math., 43 (2002), pp. 57–74.
[31] M. Discacciati and A. Quarteroni, *Convergence analysis of a subdomain iterative method for the finite element approximation of the coupling of Stokes and Darcy equations*, Comput. Vis. Sci., 6 (2004), pp. 93–103.
[32] M. Discacciati, A. Quarteroni, and A. Valli, *Robin–Robin domain decomposition methods for the Stokes–Darcy coupling*, SIAM J. Numer. Anal., 45 (2007), pp. 1246–1268, https://doi.org/10.1137/06065091X.
[33] C. M. Elliott and A. M. Stuart, *The global dynamics of discrete semilinear parabolic equations*, SIAM J. Numer. Anal., 30 (1993), pp. 1622–1663, https://doi.org/10.1137/0730084.
[34] V. J. Ervin, E. W. Jenkins, and H. Lee, *Approximation of the Stokes-Darcy system by optimization*, J. Sci. Comput., 59 (2014), pp. 775–794.
[35] V. J. Ervin, E. W. Jenkins, and S. Sun, *Coupled generalized nonlinear Stokes flow with flow through a porous medium*, SIAM J. Numer. Anal., 47 (2009), pp. 929–952, https://doi.org/10.1137/070708354.

[36] V. J. Ervin, E. W. Jenkins, and S. Sun, *Coupling nonlinear Stokes and Darcy flow using mortar finite elements*, Appl. Numer. Math., 61 (2011), pp. 1198–1222.
[37] D. J. Eyre, *Unconditionally gradient stable time marching the Cahn-Hilliard equation*, in Computational and Mathematical Models of Microstructural Evolution (San Francisco, CA, 1998), Mater. Res. Soc. Sympos. Proc., 529 (1998), pp. 39–46.
[38] W. Feng, X.-M. He, Z. Wang, and X. Zhang, *Non-iterative domain decomposition methods for a non-stationary Stokes-Darcy model with Beavers-Joseph interface condition*, Appl. Math. Comput., 219 (2012), pp. 453–463.
[39] G. J. Fix, *Phase field problems for free boundary problems*, in Free Boundary Problems: Theory and Applications, A. Fasano and M. Primicerio, eds., Pitman, Boston, 1983, pp. 580–589.
[40] J. Galvis and M. Sarkis, *Non-matching mortar discretization analysis for the coupling Stokes-Darcy equations*, Electron. Trans. Numer. Anal., 26 (2007), pp. 350–384.
[41] M. Gao and X. Wang, *An efficent scheme for a phase field model for the moving contact line problem with variable density and viscosity*, J. Comput. Phys., 272 (2014), pp. 704–718.
[42] G. N. Gatica, S. Meddahi, and R. Oyarzúa, *A conforming mixed finite-element method for the coupling of fluid flow with porous media flow*, IMA J. Numer. Anal., 29 (2009), pp. 86–108.
[43] G. N. Gatica, R. Oyarzúa, and F. J. Sayas, *A residual-based a posteriori error estimator for a fully-mixed formulation of the Stokes-Darcy coupled problem*, Comput. Methods Appl. Mech. Engrg., 200 (2011), pp. 1877–1891.
[44] V. Girault and B. Rivière, *DG approximation of coupled Navier–Stokes and Darcy equations by Beaver–Joseph–Saffman interface condition*, SIAM J. Numer. Anal., 47 (2009), pp. 2052–2089, https://doi.org/10.1137/070686081.
[45] V. Girault, D. Vassilev, and I. Yotov, *Mortar multiscale finite element methods for Stokes-Darcy flows*, Numer. Math., 127 (2014), pp. 93–165.
[46] M. Gunzburger, X.-M. He, and B. Li, *On Ritz projection and multistep backward differentiation schemes in decoupling the Stokes–Darcy model*, SIAM J. Numer. Anal., to appear.
[47] M. E. Gurtin, D. Polignone, and J. V. Nals, *Two-phase binary fluids and immiscible fluids described by an order parameter*, Math. Models Methods Appl. Sci., 6 (1996), pp. 815–831.
[48] D. Han, *Diffuse Interface Method for Two-Phase Incompressible Flows*, Ph.D. Dissertation, Florida State University, Tallahassee, FL, 2015.
[49] D. Han, *A decoupled unconditionally stable numerical scheme for the Cahn-Hilliard-Hele-Shaw system*, J. Sci. Comput., 66 (2016), pp. 1102–1121.
[50] D. Han, A. Brylev, X. Yang, and Z. Tan, *Numerical analysis of second order, fully discrete energy stable schemes for phase field models of two phase incompressible flows*, J. Sci. Comput., 70 (2017), pp. 965–989.
[51] D. Han, D. Sun, and X. Wang, *Two-phase flows in karstic geometry*, Math. Methods Appl. Sci., 37 (2014), pp. 3048–3063.
[52] D. Han and X. Wang, *Decoupled energy-law preserving numerical schemes for the Cahn-Hilliard-Darcy system*, Numer. Methods Partial Differential Equations, 32 (2016), pp. 936–954.
[53] D. Han, X. Wang, and H. Wu, *Existence and uniqueness of global weak solutions to a Cahn-Hilliard-Stokes-Darcy system for two phase incompressible flows in karstic geometry*, J. Differential Equations, 257 (2014), pp. 3887–3933.
[54] N. Hanspal, A. Waghode, V. Nassehi, and R. Wakeman, *Numerical analysis of coupled Stokes/Darcy flow in industrial filtrations*, Transp. Porous Media, 64 (2006), pp. 73–101.
[55] X.-M. He, J. Li, Y. Lin, and J. Ming, *A domain decomposition method for the steady-state Navier–Stokes–Darcy model with Beavers–Joseph interface condition*, SIAM J. Sci. Comput., 37 (2015), pp. S264–S290, https://doi.org/10.1137/140965776.
[56] P. C. Hohenberg and B. I. Halperin, *Theory of dynamic critical phenomena*, Rev. Mod. Phys., 49 (1977), pp. 435–479.
[57] R. Hoppe, P. Porta, and Y. Vassilevski, *Computational issues related to iterative coupling of subsurface and channel flows*, Calcolo, 44 (2007), pp. 1–20.
[58] J. Hou, X.-M. He, C. Guo, M. Wei, and B. Bai, *A dual-porosity-Stokes model and finite element method for coupling dual-porosity flow and free flow*, SIAM J. Sci. Comput., 38 (2016), pp. B710–B739, https://doi.org/10.1137/15M1044072.
[59] D. Jacqmin, *Calculation of two-phase Navier-Stokes flows using phase-field modeling*, J. Comput. Phys., 155 (1999), pp. 96–127.

[60] C. Kahle, *An L^∞ bound for the Cahn-Hilliard equation with relaxed non-smooth free energy*, Int. J. Numer. Anal. Model., 14 (2017), pp. 243–254.
[61] G. Kanschat and B. Riviére, *A strongly conservative finite element method for the coupling of Stokes and Darcy flow*, J. Comput. Phys., 229 (2010), pp. 5933–5943.
[62] T. Karper, K. A. Mardal, and R. Winther, *Unified finite element discretizations of coupled Darcy-Stokes flow*, Numer. Methods Partial Differential Equations, 25 (2009), pp. 311–326.
[63] J. Kim, *Phase-field models for multi-component fluid flows*, J. Comput. Phys., 12 (2012), pp. 613–661.
[64] J. S. Langer, *Models of pattern formation in first-order phase transitions*, in Directions in Condensed Matter Physics, G. Grinstein, and G. Mazenko, eds., World Scientific, Singapore, 1986, pp. 165–186.
[65] W. Layton, H. Tran, and C. Trenchea, *Analysis of long time stability and errors of two partitioned methods for uncoupling evolutionary groundwater–surface water flows*, SIAM J. Numer. Anal., 51 (2013), pp. 248–272, https://doi.org/10.1137/110834494.
[66] W. J. Layton, F. Schieweck, and I. Yotov, *Coupling fluid flow with porous media flow*, SIAM J. Numer. Anal., 40 (2002), pp. 2195–2218, https://doi.org/10.1137/S0036142901392766.
[67] R. Li, J. Li, X.-M. He, and Z. Chen, *A stabilized finite volume element method for a coupled Stokes-Darcy problem*, Appl. Numer. Math., to appear, https://doi.org/10.1016/j.apnum.2017.09.013.
[68] K. Lipnikov, D. Vassilev, and I. Yotov, *Discontinuous Galerkin and mimetic finite difference methods for coupled Stokes-Darcy flows on polygonal and polyhedral grids*, Numer. Math., 126 (2014), pp. 321–360.
[69] S. Litster, D. Sinton, and N. Djilali, *Ex situ visualization of liquid water transport in PEM fuel cell gas diffusion layers*, J. Power Source, 154 (2006), pp. 95–105.
[70] C. Liu and J. Shen, *A phase field model for the mixture of two incompressible fluids and its approximation by a Fourier-spectral method*, Phys. D, 179 (2003), pp. 211–228.
[71] C. Liu, J. Shen, and X. Yang, *Decoupled energy stable schemes for a phase-field model of two-phase incompressible flows with variable density*, J. Sci. Comput., 62 (2015), pp. 601–622.
[72] J. Lowengrub and L. Truskinovsky, *Quasi-incompressible Cahn-Hilliard fluids and topological transitions*, R. Soc. Lond. Proc. Ser. A Math. Phys. Eng. Sci., 454 (1998), pp. 2617–2654.
[73] L. Ma, R. Chen, X. Yang, and H. Zhang, *Numerical approximations for Allen-Cahn type phase field model of two-phase incompressible fluids with moving contact lines*, Comm. Comput. Phys., 21 (2017), pp. 867–889.
[74] A. Márquez, S. Meddahi, and F. J. Sayas, *Strong coupling of finite element methods for the Stokes-Darcy problem*, IMA J. Numer. Anal., 35 (2015), pp. 969–988.
[75] A. Masud and T. J. R. Hughes, *A stabilized mixed finite element method for Darcy flow*, Comput. Methods Appl. Mech. Eng., 191 (2002), pp. 4341–4370.
[76] M. Mu and J. Xu, *A two-grid method of a mixed Stokes–Darcy model for coupling fluid flow with porous media flow*, SIAM J. Numer. Anal., 45 (2007), pp. 1801–1813, https://doi.org/10.1137/050637820.
[77] M. Mu and X. Zhu, *Decoupled schemes for a non-stationary mixed Stokes-Darcy model*, Math. Comp., 79 (2010), pp. 707–731.
[78] S. Münzenmaier and G. Starke, *First-order system least squares for coupled Stokes-Darcy flow*, SIAM J. Numer. Anal., 49 (2011), pp. 387–404, https://doi.org/10.1137/100805108.
[79] R. H. Nochetto, A. J. Salgado, and S. W. Walker, *A diffuse interface model for electrowetting with moving contact lines*, Math. Models Methods Appl. Sci., 24 (2014), pp. 67–111.
[80] T. Qian, X. Wang, and P. Sheng, *Generalized Navier boundary condition for the moving contact line*, Commun. Math. Sci., 1 (2003), pp. 333–341.
[81] T. Qian, X. Wang, and P. Sheng, *Molecular scale contact line hydrodynamics of immiscible flows*, Phys. Rev. E, 68 (2003), 016306.
[82] T. Qian, X. Wang, and P. Sheng, *Power-law slip profile of the moving contact line in two phase immiscible flows*, Phys. Rev. Lett., 63 (2004), 094501.
[83] B. Rivière and I. Yotov, *Locally conservative coupling of Stokes and Darcy flows*, SIAM J. Numer. Anal., 42 (2005), pp. 1959–1977, https://doi.org/10.1137/S0036142903427640.
[84] L. Shan and H. Zheng, *Partitioned time stepping method for fully evolutionary Stokes–Darcy flow with Beavers–Joseph interface conditions*, SIAM J. Numer. Anal., 51 (2013), pp. 813–839, https://doi.org/10.1137/110828095.

[85] J. Shen and X. Yang, *An efficient moving mesh spectral method for the phase-field model of two-phase flows*, J. Comput. Phys., 228 (2009), pp. 2978–2992.
[86] J. Shen and X. Yang, *A phase-field model and its numerical approximation for two-phase incompressible flows with different densities and viscosities*, SIAM J. Sci. Comput., 32 (2010), pp. 1159–1179, https://doi.org/10.1137/09075860X.
[87] J. Shen and X. Yang, *Energy stable schemes for Cahn-Hilliard phase-field model of two-phase incompressible flows*, Chin. Ann. Math. Ser. B, 31 (2010), pp. 743–758.
[88] J. Shen and X. Yang, *Numerical approximations of Allen-Cahn and Cahn-Hilliard equations*, Discrete Contin. Dyn. Syst., 28 (2010), pp. 1169–1691.
[89] J. Shen and X. Yang, *Decoupled energy stable schemes for phase filed models of two phase complex fluids*, SIAM J. Sci. Comput., 36 (2014), pp. B122–B145, https://doi.org/10.1137/130921593.
[90] J. Shen and X. Yang, *Decoupled, energy stable schemes for phase-field models of two-phase incompressible flows*, SIAM J. Numer. Anal., 53 (2015), pp. 279–296, https://doi.org/10.1137/140971154.
[91] J. Shen, X. Yang, and Q. Wang, *On mass conservation in phase field models for binary fluids*, Comm. Comput. Phys, 13 (2012), pp. 1045–1065.
[92] J. Shen, X. Yang, and H. Yu, *Efficient energy stable numerical schemes for a phase-field moving contact line model*, J. Comput. Phys., 284 (2015), pp. 617–630.
[93] S. Tlupova and R. Cortez, *Boundary integral solutions of coupled Stokes and Darcy flows*, J. Comput. Phys., 228 (2009), pp. 158–179.
[94] D. Vassilev, C. Wang, and I. Yotov, *Domain decomposition for coupled Stokes and Darcy flows*, Comput. Methods Appl. Mech. Engrg., 268 (2014), pp. 264–283.
[95] G. Wang, Y. He, and R. Li, *Discontinuous finite volume methods for the stationary Stokes-Darcy problem*, Internat. J. Numer. Methods Engrg., 107 (2016), pp. 395–418.
[96] C. Xu and T. Tang, *Stability analysis of large time-stepping methods for epitaxial growth models*, SIAM J. Numer. Anal., 44 (2006), pp. 1759–1779, https://doi.org/10.1137/050628143.
[97] X. Yang, *Error analysis of stabilized semi-implicit method of Allen-Cahn equation*, Disc. Conti. Dyn. Sys.-B, 11 (2009), pp. 1057–1070.
[98] X. Yang, *Linear, first and second order and unconditionally energy stable numerical schemes for the phase field model of homopolymer blends*, J. Comput. Phys., 327 (2016), pp. 294–316.
[99] X. Yang, J. J. Feng, C. Liu, and J. Shen, *Numerical simulations of jet pinching-off and drop formation using an energetic variational phase-field method*, J. Comput. Phys., 218 (2006), pp. 417–428.
[100] X. Yang, M. G. Forest, H. Li, C. Liu, J. Shen, Q. Wang, and F. Chen, *Modeling and simulations of drop pinch-off from liquid crystal filaments and the leaky liquid crystal faucet immersed in viscous fluids*, J. Comput. Phys., 236 (2013), pp. 1–14.
[101] X. Yang and L. Ju, *Efficient linear schemes with unconditionally energy stability for the phase field elastic bending energy model*, Comput. Meth. Appl. Mech. Engrg., 315 (2017), pp. 691–712.
[102] H. Yu and X. Yang, *Numerical approximations for a phase-field moving contact line model with variable densities and viscosities*, J. Comput. Phys., 334 (2017), pp. 665–686.
[103] P. Yue, J. Feng, C. Liu, and J. Shen, *A diffuse-interface method for simulating two-phase flows of complex fluids*, J. Fluid Mech., 515 (2004), pp. 293–317.
[104] J. Zhao, H. Li, Q. Wang, and X. Yang, *A linearly decoupled energy stable scheme for phase-field models of three-phase incompressible flows*, J. Sci. Comput., 70 (2017), pp. 1367–1389.
[105] J. Zhao, Q. Wang, and X. Yang, *Numerical approximations to a new phase field model for immiscible mixtures of nematic liquid crystals and viscous fluids*, Comput. Meth. Appl. Mech. Eng., 310 (2016), pp. 77–97.
[106] J. Zhao, Q. Wang, and X. Yang, *Numerical approximations for a phase field dendritic crystal growth model based on the invariant energy quadratization approach*, Inter. J. Num. Meth. Engrg., 110 (2017), pp. 279–300.
[107] J. Zhu, L. Q. Chen, J. Shen, and V. Tikare, *Morphological evolution during phase separation and coarsening with strong inhomogeneous elasticity*, Model. Simul. Mater. Sci. Eng., 9 (2001), pp. 499–511.